Praktikum: NanoCharakterization I

Transmission Electron Microscopy

Instrumentation, Basic Operation Modes, Resolution, Electron Diffraction and its Applications, Contrast Mechanism and High-Resolution Imaging

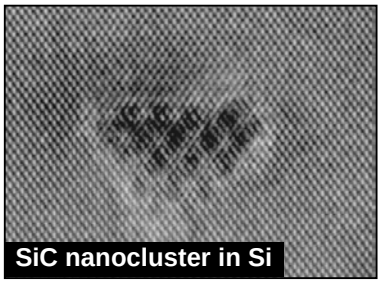
SiC nanocluster in Si

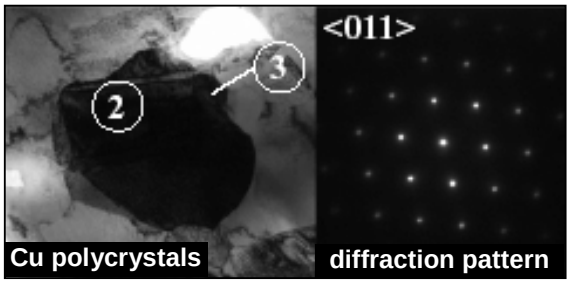

Cu polycrystals diffraction pattern

Contents

Transmission Electron Microscopy

1.1 Basic Features of TEM

- Electron energies typically in the range of 100 … 300 keV, up to 3 MeV.
- Transmission of thin sample specimen with thickness of < 100 nm due to small penetration depth: Images correspond to the projection of the whole sample cross-section onto the image plane.
- Magnification: 500 – 500.000, resolution down to ~1 Å,
- Two types: (i) projection imaging TEM or (ii) scanning *transmission* electron microscope STEM.

Advantages:
- **Very high resolution** (~ 1 - 4 Å): ⇨ Lateral resolution of single atomic columns.
- Very **high sensitivity** to ***lattice distortions***, crystal orientation, structural defects, etc.
- Can be combination with **high resolution chemical microanalysis** (EDX, EELS…)

Disadvantages:
- Little surface sensitivity due averaging over whole sample thickness.
- Averaging over transmitted sample thickness („atoms“ = atom columns).
- Time consuming and difficult sample preparation due to required thin sample thickness.
- Radiation damage of the samples due to high electron energy and dose.
- High voltages and vacuum conditions required.
- Complicated contrast mechanisms, dynamical diffraction, multiple scattering:
  ⇨ to completely understand TEM images and their contrast image simulations are required.

1.2 TEM Components and Instrumentation

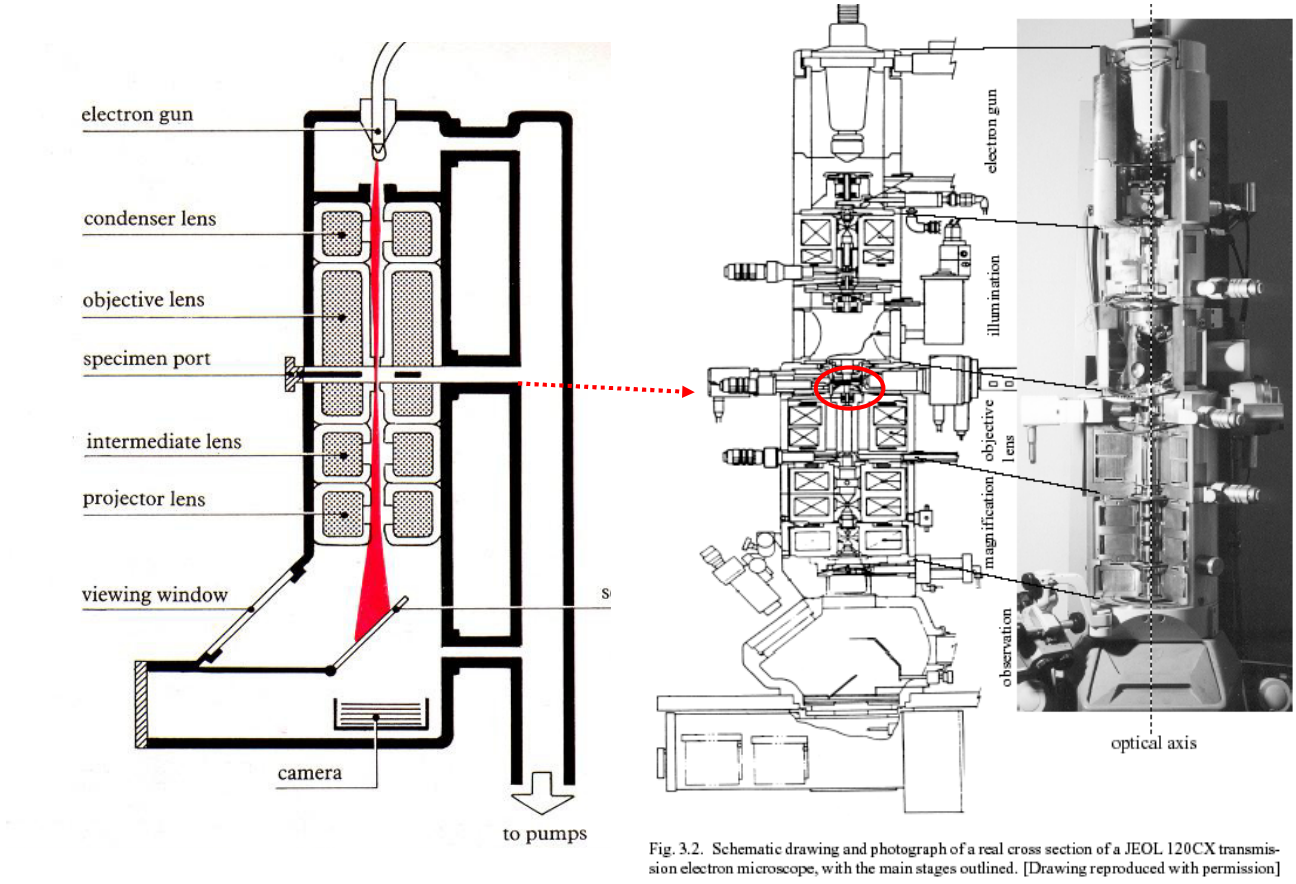

Fig. 3.2. Schematic drawing and photograph of a real cross section of a JEOL 120CX transmission electron microscope, with the main stages outlined. [Drawing reproduced with permission]

Electro optical column:

- Electron source and electron gun.
- Condenser optics to define and manipulate the electron beam on the sample (condenser lenses, apertures and deflection coils).
- Sample holder and manipulator (rocking, translation, heating, cooling ..).
- Sample load lock entry port.
- Image formation objective, intermediate, projection lenses with small aberration constants.
- Diffraction and selective area apertures.
- Viewing screen, viewing window, CCD camera, photo plates.

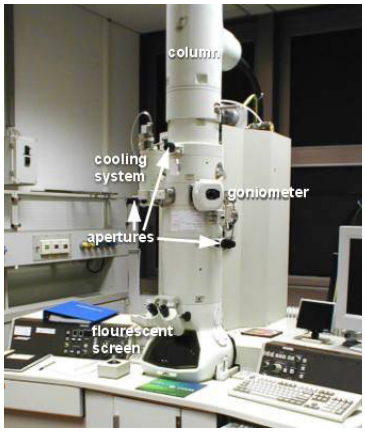

Control system:

- HV supply, individual control of each lens and deflection coils.
- Optional computer control system.

Vacuum system:

$p < 10^{-6}$ mbar, mean free electron path >> optical path.

- Column = vacuum chamber, vacuum pumps, vacuum gauges & control
- Optional: vibration insulation.

Sample preparation:

- Sample thinning by polishing, grinding, ion-beam sputtering, chemical methods, ultramicrotomy, etc…
- Maximal sample thickness ~ 100 … 300 nm, depending on density and electron energy.

1.2.1 Sample Holders and Support Grids

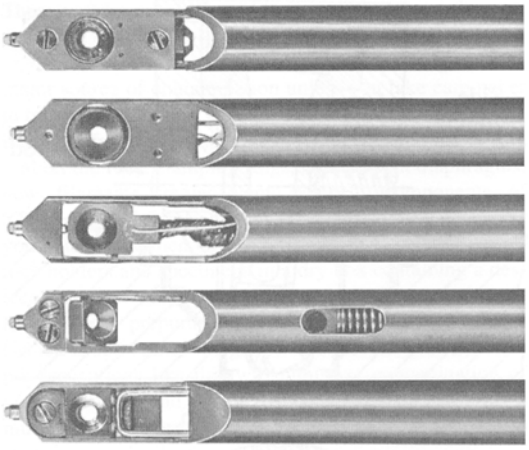

Figure 8.8. Examples of different designs for the side-entry holder. From the top, they are: a rotation holder, a heating holder, a cooling holder, a double-tilt holder, and a single-tilt holder.

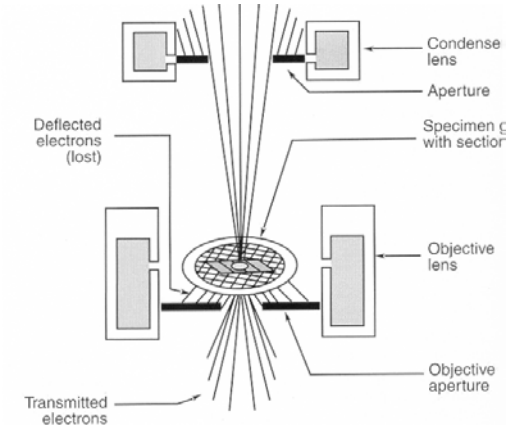

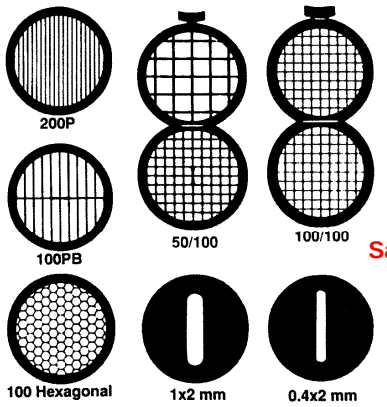

Figure 10.2. A variety of specimen support grids of different mesh size and shape. At the top right is the oyster grid, useful for sandwiching

Sample Grids:

Supporting grid material:

- ❖ Low Z number to reduce scattering and x-ray emission.
- ❖ High mechanical strength and low thermal expansion.
- ❖ Good electrical conductivity to avoid charging.
- ❖ Good thermal conductivity to prevent heating.
- ❖ Resistance to electron radiation.

1.2.2 The Illumination System

Consists of two condenser lenses C1 and C2, two deflection coils, an aperture at the C2 lens and the upper part of the objective lens.

Purpose:

- ❖ Homogeneous illumination of the sample area that is used for image formation in dependence of the sample magnification.
- ❖ C2 aperture can be used to adjust the beam current.
- ❖ Parallel beam or convergent beam illumination.
- ❖ Spatial coherence maximized for parallel beam illumination.
- ❖ Translating and tilting the beam with respect to the optical axis of the column.
- ❖ STEM: point spot and scanning realized with scan coils.

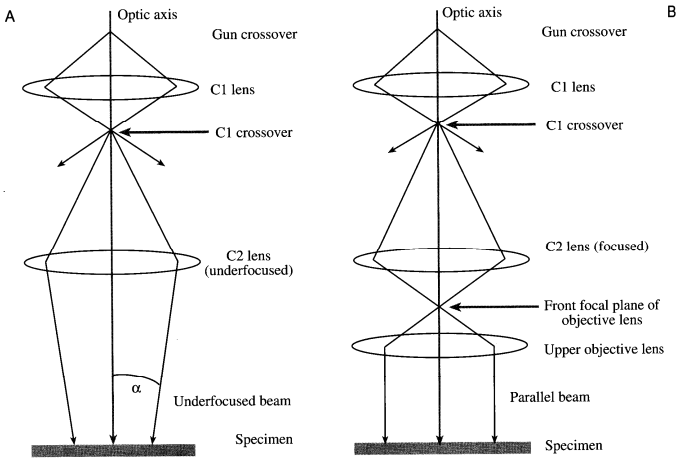

Figure 9.1. Parallel-beam operation in the TEM (A) using just the C1 and an underfocused C2 lens and (B) using the C1 and C2 lenses to image the source at the front focal plane of the upper objective lens.

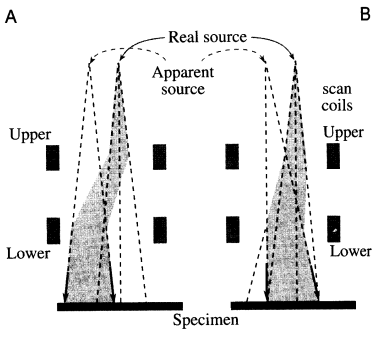

1.3 Basic TEM Operation Modes

A. Diffraction mode

At the focus of the objective lens all *parallel beams* emitted from the sample are focused on the same point. Thus, a diffraction pattern of the electrons transmitted through the sample is formed at the objective back focal plane.

Setting the focal length of the intermediate lens so that this diffraction pattern is focused on the second intermediate image and final projector lens, the diffraction pattern is magnified onto the viewing screen.

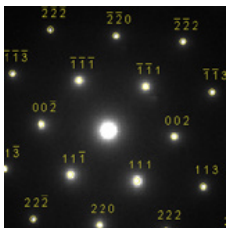

Electron diffraction pattern

B. Imaging mode

In this case, the **intermediate lens** is set such that the real intermediate image 1 that is formed at the image plane of the objective lens is projected to the object plane of the final projector lens, which is then magnified onto the final viewing screen.

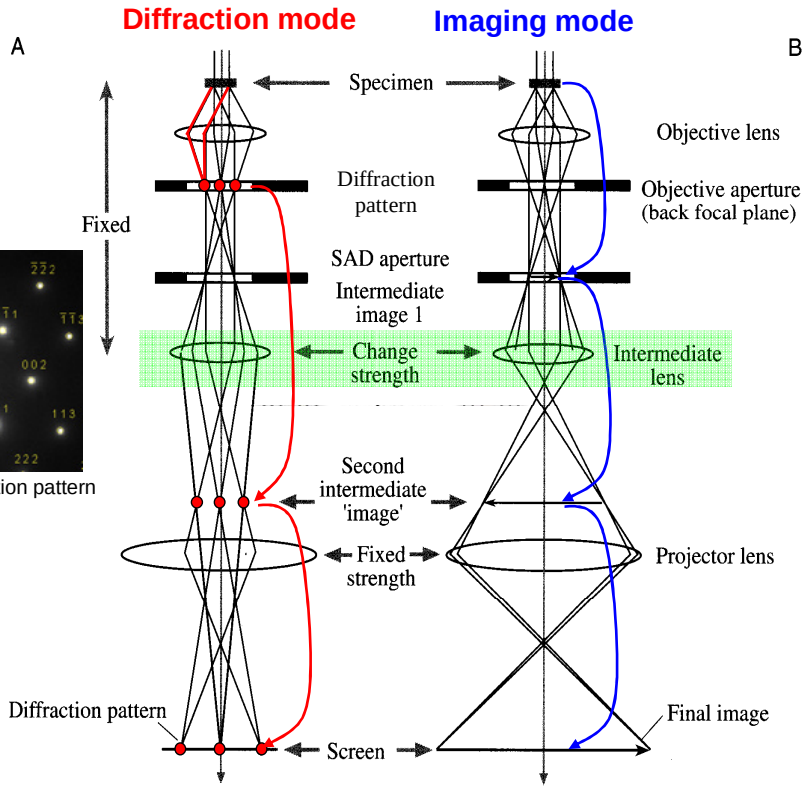

⇨ By changing the focal length of an intermediate lens, one can choose between the diffraction pattern (back focal plane) or the image (in the image plane).

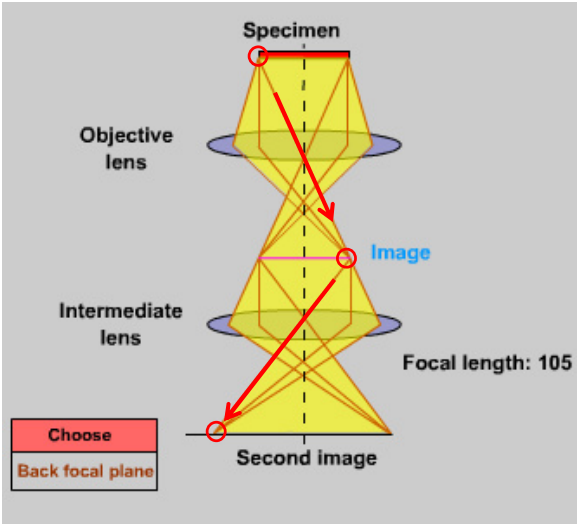

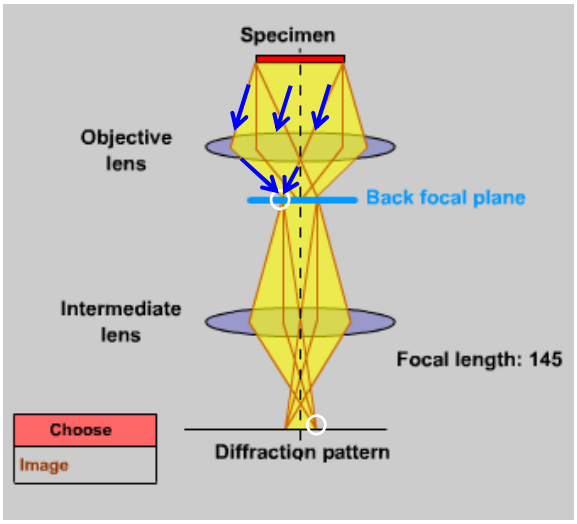

Diffraction mode:

- Yields information on the crystallinity, **crystal structure** and **orientation** of the illuminated sample area.
- Used to **identify sample material** and **composition**.
- Selection of specific scattering components used for TEM image formation using the movable objective aperture.
- Adjustment of the contrast mechanisms in the TEM images.
- Definition of the sample area contributing to the diffraction pattern by using the selective area aperture (SAD).

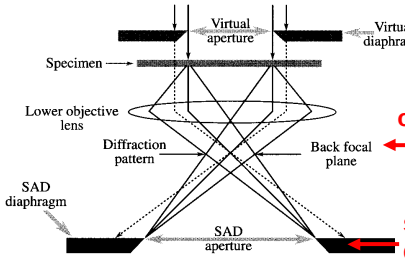

Figure 9.13. Ray diagram showing SAD pattern formation: the insertion of an aperture in the image plane results in the creation of a virtual aperture in the plane of the specimen. Only electrons falling inside the dimensions of the virtual aperture at the specimen will be allowed through into the imaging system. All other electrons will hit the SAD diaphragm.

Imaging modes:

- Using the **objective aperture**, different parts of the diffraction image can be used for image formation.
- **Bright field imaging**: TEM image formed by using only the direct electron beam in of the diffraction pattern.
- **Dark field imaging**: only certain diffraction spots are selected for image formation. In this image mode there is a very high sensitivity to the crystal structure and lattice deformations in the sample.
- To minimize aberration effects in dark field imaging, the **centered dark field mode** is used in which the diffracted spot is moved to the center of the optical axis by tilting the sample.

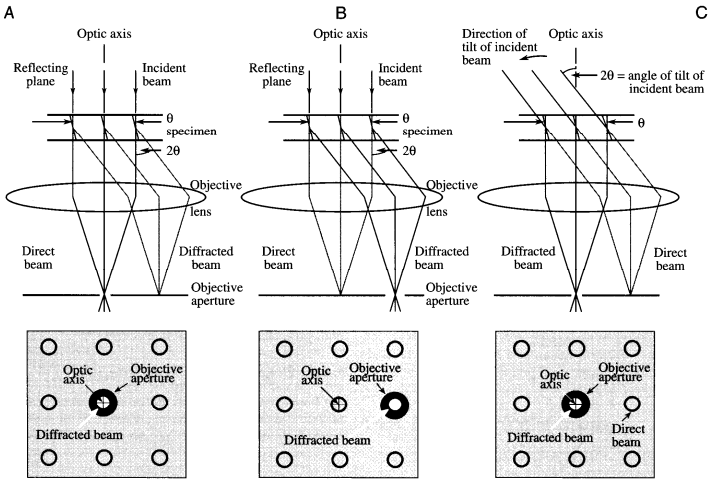

Figure 9.14. Ray diagrams showing how the objective lens/aperture are used in combination to produce (A) a BF image formed from the direct beam, (B) a displaced-aperture DF image formed with a specific off-axis scattered beam, and (C) a CDF image where the incident beam is tilted so that the scattered beam remains on axis. The area selected by the objective aperture, as seen on the viewing screen, is shown below each ray diagram.

1.4 TEM Resolution

As for all microscopy methods (see Chapt. 4), the **resolution of TEM is limited** by two factors

(i) diffraction where $r_{diff} \sim \frac{1}{2}\,\lambda/\sin\alpha$, as well as by **(ii) lens aberrations** where $r_{aber} \sim C_{lens}\,\alpha^{n}$,

Total effective resolution is given by:

$$r_{tot} = (r_{diff}^2 + r_{shp}^2 + r_{chr}^2 + r_{ast}^2)^{1/2}$$

$$r_{diff} = 0.61 \cdot \lambda / n \sin\alpha$$

Using $\sin\alpha \approx \alpha$, this yields:

$$r_{tot} = [\,(0.61 \cdot \lambda/\alpha)^2 + (C_{sph}\cdot\alpha^3)^2 + (C_{chr}\cdot\Delta E/E \cdot \alpha)^2\,]^{1/2}$$

α = aperture angle, C_{sph} and C_{chr} are the spherical and chromatic aberration constants.

⇨ **With increasing aperture α** the diffraction broadening decreases but the broadening due to the lens aberration increases.

⇨ When the lens aberrations cannot be neglected, there exists a certain ***optimum aperture angle*** α_{opt} where the ***highest resolution*** is achieved !

⇨ This ***applies to all microscopy methods***.

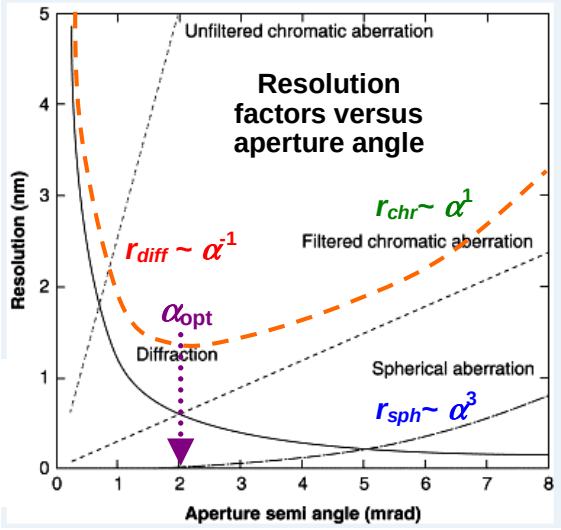

Electron microscope resolution as a function of scattering angle due to diffraction, spherical aberration, and chromatic aberration. Calculated for E =300 keV, $\Delta E_{unfiltered}$= 250 eV, $\Delta E_{filtered}$= 30eV, C_s = 3.2 mm, C_c = 3.0 mm, and f_{obj} = 3.9 mm.

Resulting TEM Resolution:

plotted as a function of:

- aperture angle α,
- lens aberrations *C*
- electron energy *E*

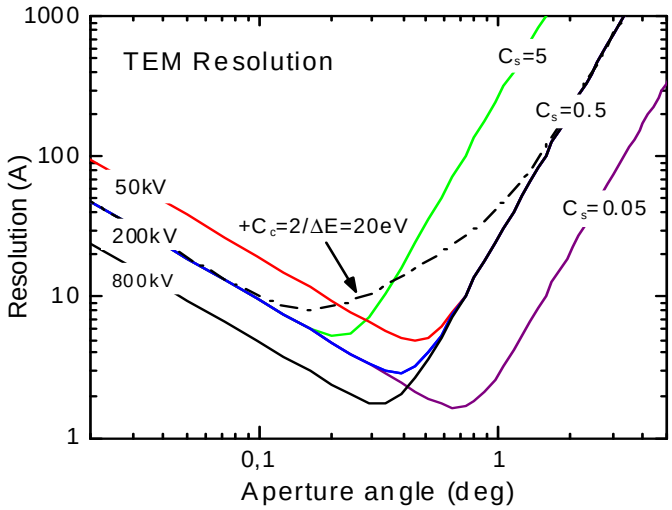

⇨ **Maximum (best) resolution:**

= minimum of r_{tot} neglecting chromatic & astigmatic aberrations

$dr_{tot}/d\alpha = 0$: » $\alpha_{opt} = 0.77\ \text{mrad} \cdot (\lambda / C_{sph})^{1/4}$ and $r_{best} = 0.91 \cdot (C_{sph} \cdot \lambda^3)^{1/4}$ at $\alpha = \alpha_{opt}$

Example: 200 keV, $\lambda = 0.0274$ Å, $C_{sph} = 0.5$ mm: » $\alpha_{opt} = 6.6$ mrad = 0.38° » $r_{best} = 2.9$ Å

⇨ **Chromatic aberration**: $\Delta E = 20$eV; 200 keV, $C_{chr} = 2$ mm: At $\alpha_{opt} = 6.6$ mrad » $r_{eff} = 13.5$ Å

- Chromatic aberration broadening can be minimized by (i) using higher electron energies (ΔE/E) and (ii) using as thin as possible specimen thickness. This is essential for high resolution.
- From Bethe equation: dE/dx = 1… 3 eV per nm for 100 keV electrons (depending on material) !

Ultra-High Resolution TEM with sub-Ångstrom resolution

TEM Resolution is mainly limited spherical aberration: $r_{min} = 0.91 \cdot (C_{sph} \cdot \lambda^3)^{1/4}$

» Resolution can be improved only by (a) decreasing the wavelength (=MeV TEMs) and/or

(b) and/or improvements in lens optics (aberration corrections).

Aberration corrections:

Scherzer (1936): Spherical aberrations cannot be avoided using rotationally symmetric electromagnetic fields !

Rose (1990ies): Spherical aberration corrections possible by using multipole fields that produce *negative* third order spherical aberrations for compensation.

» Development of hexapole and octopole correction lenses that can reduce C_{sph} to almost zero.

Additional measures for HR-TEM:

- Introduction of energy filters in the condenser system improve the monochromaticity of the electron beam and thus reduce chromatic aberrations.
- Post sample energy filter (Omega filter
- Improved mechanical construction to reduce vibration and thermal drifts of the TEM column.
- Improved stability and reduction of noise level of lens and gun currents.

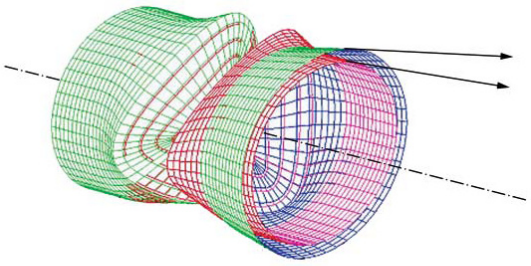

Figure 2 : Ray path through the hexapole Cs-corrector consisting of two hexapoles (rectangular boxes), which are separated by a telecentric round lens couple. It can be seen that the outer ray-path (green) is tilted away from the optical axis in order to compensate for the spherical aberration of the objective lens. Figure courtesy of Dr. S. Uhlemann, CEOS GmbH.

Resolution of Aberration Corrected TEM achieved with Multipole Correction Lenses

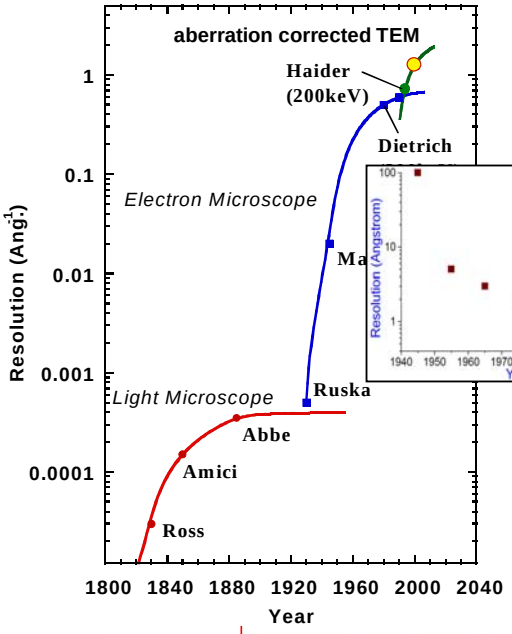

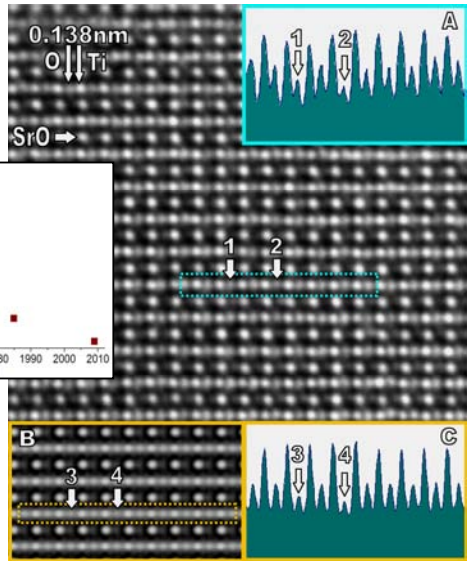

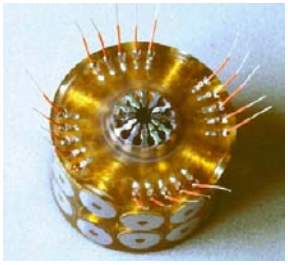

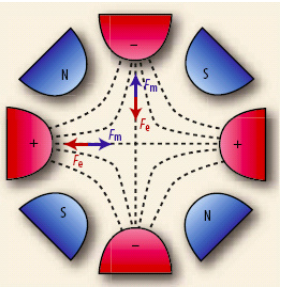

C.L. Jia, M. Lentzen and K. Urban, Science 299, 870 (2003).

Multipole Correction Lenses yields C_s values as low as µm

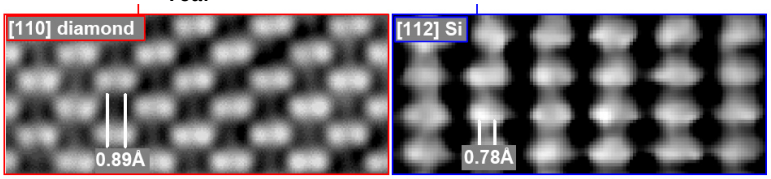

Fig. 1. Test specimens can provide separations of atom columns in atomic "dumbbells" ranging from 1.62Å to 0.51Å for samples in [110] and [112] orientations. Images obtained on the OÅM [4] show the 0.89Å carbon atom spacing in [110] diamond (left) and the 0.78Å silicon atom spacing (barely) in [112] silicon (right).

Sub-Ångstrom resolution can be achieved by modern aberration corrected ultra-high resolution TEMs !

Examples for high resolution TEMs:

FEI Titan HR-TEM

Figure 1: FEI Titan™ 80-300. (Unless noted otherwise, all images below were acquired with the Titan™ 80-300)

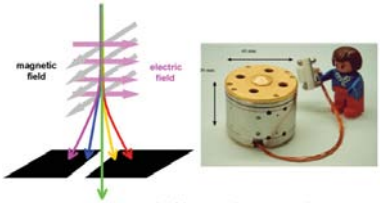

Figure 3: The principle of the monochromator with a picture of a Wien-filter type monochromator

Zeiss UR-TEM

Figure 1. Carl Zeiss SMT's new sub-Angstrom UHRTEM with revolutionary column suspension concept

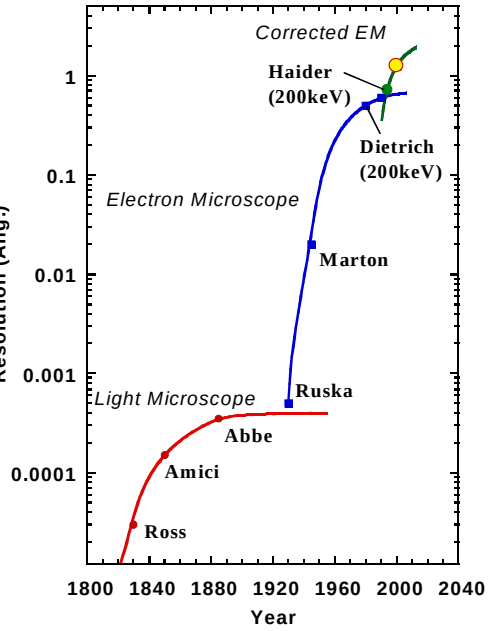

Performance comparison for high resolution TEMs:

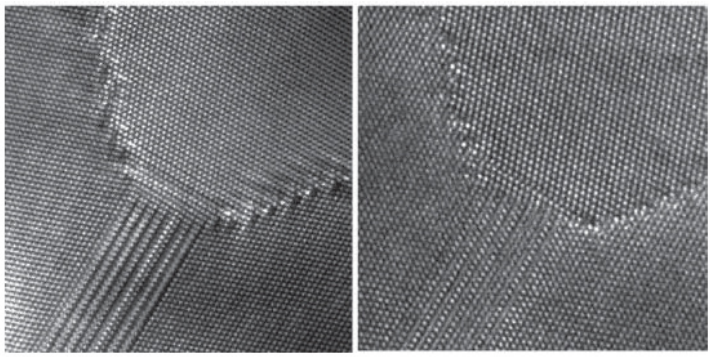

Figure 4. Comparison of a not Cs-corrected (left) and a Cs-corrected (right) HR-TEM image on the same area of a polycrystalline gold sample in <110> direction. The delocalisation due to spherical aberration is visible at the grain boundary in the uncorrected image (left). The exact positions of the atoms on the grain boundary can be clearly seen in the Cs-corrected image (right), while Móire patterns are degrading the resolution in the uncorrected image (left). Sample courtesy: C. Kisielowski, from the National Center of Microscopy in Berkeley, USA

Figure 3. Image of Au particles on carbon support film. With an uncorrected objective lens (a) string delocalisation (fringe contrast outside the particles) is visible. In the Cs-corrected case (b) the delocalisation has dissapeared and the Au particle is imaged artefact free

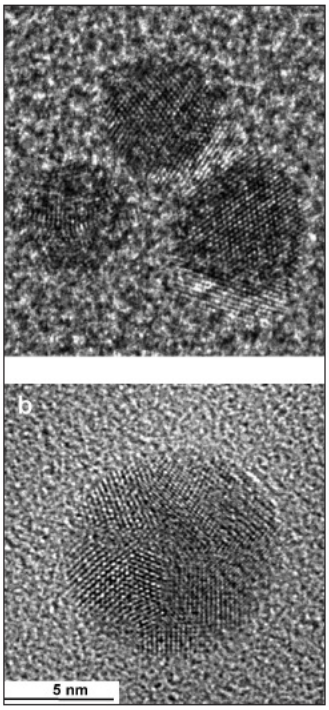

References
1. O Scherzer, Z Physik 101 (1936), 593-603
2. H Rose, Optik 85 (1990), 19-24

Performance of high resolution TEMs:

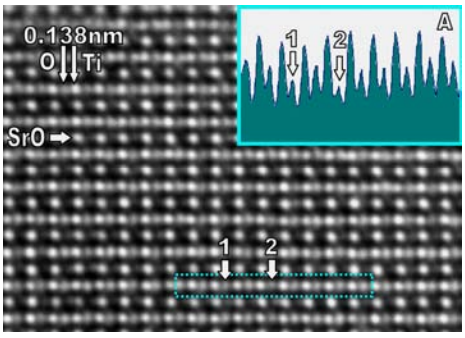

C.L. Jia, et al., Science 299, 870 (2003).

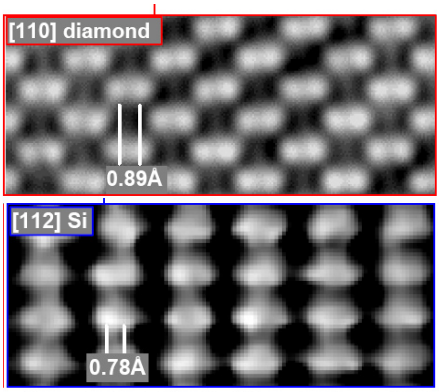

Fig. 1. Test specimens can provide separations of atom columns in atomic "dumbbells" ranging from 1.62Å to 0.51Å for samples in [110] and [112] orientations. Images obtained on the OÅM [4] show the 0.89Å carbon atom spacing in [110] diamond (left) and the 0.78Å silicon atom spacing (barely) in [112] silicon (right).

Imaging of lomer type dislocation cores in GaAs

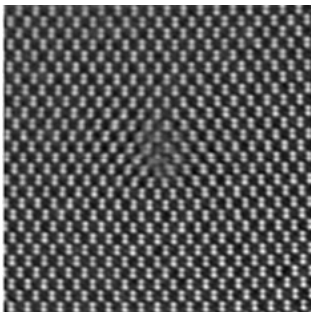

igh-resolution image of a pure edge dislocation of Lomer type with **b** = a/2 [110] located at the interface between a GaAs substrate (below) and a lattice mismatched InGaAs epilayer.The image shows the phase of the exit-plane wave function as retrieved from a through-focus series of experimental images taken with the centre's aberration corrected Philips CM-200 electron microscope. Due to an information limit well below 1.3 Ångström atomic column positions right up to the dislocation core are clearly resolved. A single detached atomic column at the images centre directly reveals the existence of dislocation

Local deformation of GaAs near stacking faults

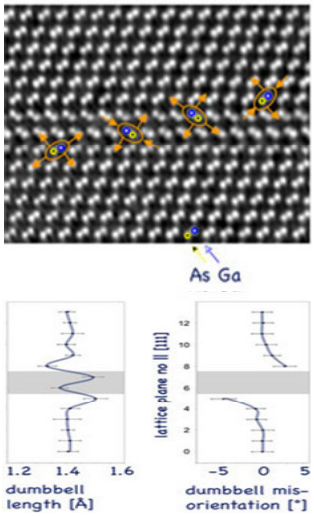

Locally inhomogeneous distortions of gallium and arsenic atomic dumbbells in the vicinity of a faulted double stacking fault ribbon in GaAs viewed along the [110] zone axis.

The top image displays a phase image evaluated from a through focus series of 15 experimental micrographs. In the phase image, atomic column positions are superimposed and dumbbell distortions are indicated exemplarily in dependence on specific positions along the crystallographic [111] direction.

The lower graphs display measured average projected bond length and misorientation angles of the dumbbells along the (111) direction. The lattice planes belonging to the double stacking fault ribbon are indicated in lighter grey colour

K. Tillmann, A. Thust and K. Urban

1.4 Mangification and Depth of Field and Depth of Focus

Magnification *M*: For each lens, the magnification *M* is given by $M = L_i / L_o$;

where, L_i and L_o are the image, respectively, object distances from the lens, which can be adjusted by changes in the strength of the magnetic lenses.

The total magnification is given by the product of all lens magnification factors.

Practically, the actual magnification of any microscope must be calibrated because it depends on:

- ❖ The actual sample position on the optical axis, as well as rotation and tilt of the sample (± 5%).
- ❖ Lens uncertainties: current & hysteresis (±1%).
- ❖ Camera length.

» The error of the actual magnification with respect to the nominal value can be as large as 10%.

» Requires calibration using grating standards or atomically resolved lattice images.

Depth of image *S* is given by: $S = \delta_s \cdot M^2 / \alpha_0$,

where δ_s is the lateral resolution and *M* is the magnification.

Due to the large magnification and small apertures α in TEM the depth of image is larger than several meters !

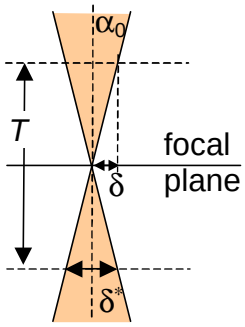

Depth of focus *T* is given by: $T = \delta_s / \alpha_0$

For a required lateral resolution of 2 Å, the depth of focus is typically 20 nm. This limits the maximal allowable sample thickness.

1.5 Electron Diffraction

In TEM, electron diffraction is an important tool in order to identify local materials in the sample, determine the sample orientation and adjust the contrast in dark or bright field imaging.

Diffraction can be described in terms of **Braggs law** or by the **Laue condition**. Diffraction spots appear when:

$2 \cdot d_{hkl} \cdot \sin\theta_{hkl} = n \cdot \lambda$ or when $\Delta k = g^*_{hkl}$

where: d_{hkl} is the lattice spacing of the *hkl* lattice planes, θ is the diffraction angle, λ the wavelength, and Δk is the scattering vector and g^*_{hkl} the reciprocal lattice vector of the *hkl* plane.

For kinematic diffraction, the diffraction patterns can be obtained by the **Ewald construction**, which is a graphical representation of the energy and momentum conservation required in elastic scattering and diffraction. This means that:

(a) $|k_0| = |k'|$: all scattered wave vectors ***k'*** must lie on an Ewald sphere with a radius k_0,

(b) the momentum must be conserved by $\Delta k = g^*_{hkl}$.

In contrast to x-ray diffraction, for electron diffraction $|k_0| >> |g^*|$. Thus, the diffraction angles are very small $\theta_{hkl} < 0.5°$

When k_0 is very large and the diffraction angles small, the curvature of the Ewald sphere is very small, *i.e.,* the Ewald construction can be approximated by a plane cross-section through reciprocal space.

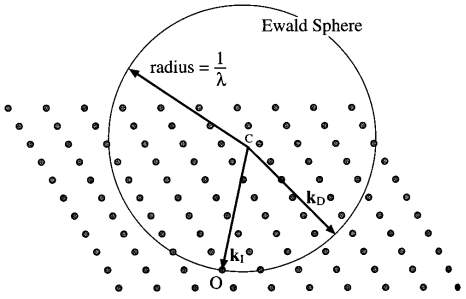

Figure 12.3. The Ewald sphere of reflection is shown intersecting a noncubic array of reciprocal-lattice points. The vector **CO** represents $\mathbf{k}_I$, the wave vector of the incident wave, and O is the origin of the reciprocal lattice. $\mathbf{k}_D$ is any radius vector. When the radius of the sphere is similar to the spacing between the points in the reciprocal lattice, as is the case for X-rays, the sphere can only intersect a few points, as shown. When λ is much smaller, as for 100-keV electrons, the radius is much larger, the sphere is flatter, and it intersects many more points.

1.5.1 The Shape of the Reciprocal Lattice Points

- Due to structural imperfections as well as finite size effects, the reciprocal lattice points are not infinitessimal small but have a certain width. The shape of the reciprocal lattice points is given by the Fourier transform of the crystal shape function.

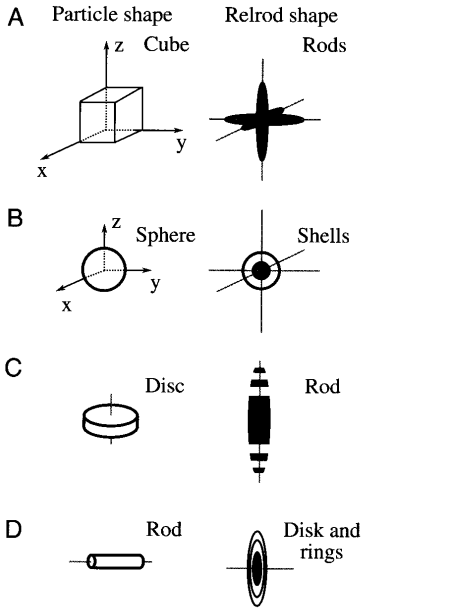

Figure 17.9. Examples of how spots in reciprocal space have different shapes, depending on the shape of the particles which are diffracting.

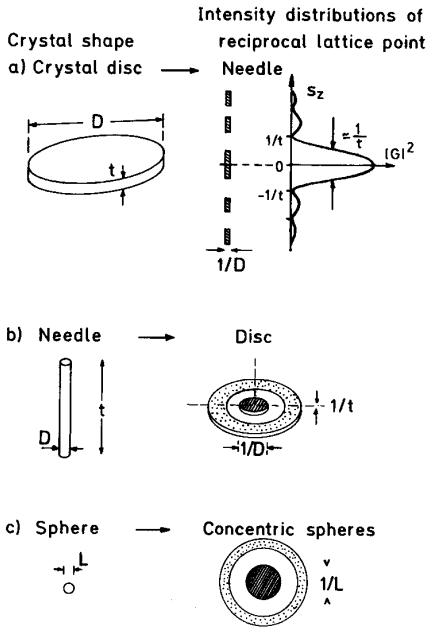

Scattering function for a row of atoms with finite number N_x

$$\left| \sum_{n_x=0}^{n_x=N-1} e^{i2\pi n_x \mathbf{K}\cdot\mathbf{a}} \right|^2 = \frac{1-\cos\,(2\pi N_x \mathbf{K}\cdot\mathbf{a})}{1-\cos\,(2\pi\,\mathbf{K}\cdot\mathbf{a})}$$

Fig. 7.10. Shape of the square of the lattice amplitude $|G|^2$ with which reciprocal lattice points have to be convolved for (**a**) a crystal disc (thin foil of thickness t), (**b**) a needle of length t and (**c**) a sphere of diameter L

1.5.2 The Ewald Construction for High-Energy Electron Diffraction

- Due to the energy spread ΔE and the angular divergence, the Ewald sphere is not infinitesimal thin.
- Likewise, the diffraction spots exhibit a significant elongation along the sample normal direction.
- Thus: always many different diffraction spot appear at the same time in the diffraction pattern.

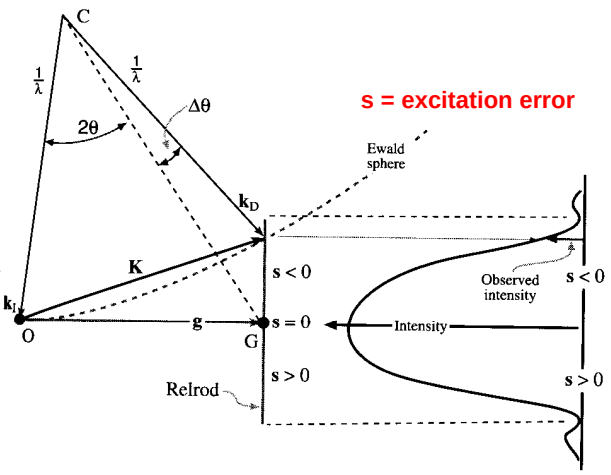

Figure 17.2. The relrod at $\mathbf{g}_{hk\ell}$ when the beam is Δθ away from the exact Bragg condition. The Ewald sphere intercepts the relrod at a negative value of s which defines the vector $\mathbf{k} = \mathbf{g} + \mathbf{s}$. The intensity of the diffracted beam as a function of where the Ewald sphere cuts the relrod is shown on the right of the diagram. In this case the intensity has fallen almost to zero.

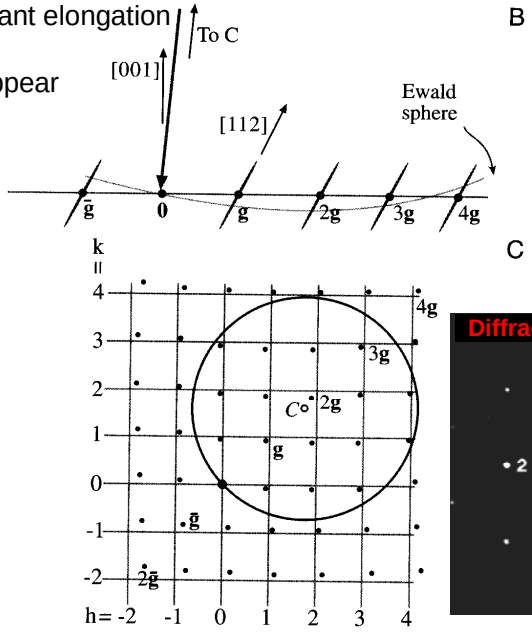

Figure 17.3. (A) For a thin specimen, every point is replaced by a relrod. (B) The Ewald sphere cutting the relrods in (A) when the crystal is tilted slightly off the 001 axis. (C) The effect of the tilt in (B) on the DP. Notice that all of the spots in the DP are displaced relative to their positions on the square grid (the projection of the spots at zero tilt), but that the magnitude of the displacement varies depending on the sign and size of s. Of course, spots on the Ewald sphere must still be the "correct" distance from 000.

Excitation Error *s*:

The excitation error *s* (see figure on previous page) is a measure for how far the center of the diffraction spot is away from the Ewald sphere, i.e., how far the diffraction deviates from the exact Bragg condition.

Higher order Laue zones:

Under favorable conditions more than the 0th order Laue zone (ZOLZ) can be observed in the diffraction patterns as shown on the right hand side.

From these higher order Laue zones information on the structure perpendicular to the specimen surfrace, i.e. along the electron beam can be obtained.

The intensity of the higher Laue zones rapidly decreases with increasing diffraction angle. The intensity can be enhanced by illumination of the sample with a convergent electron beam.

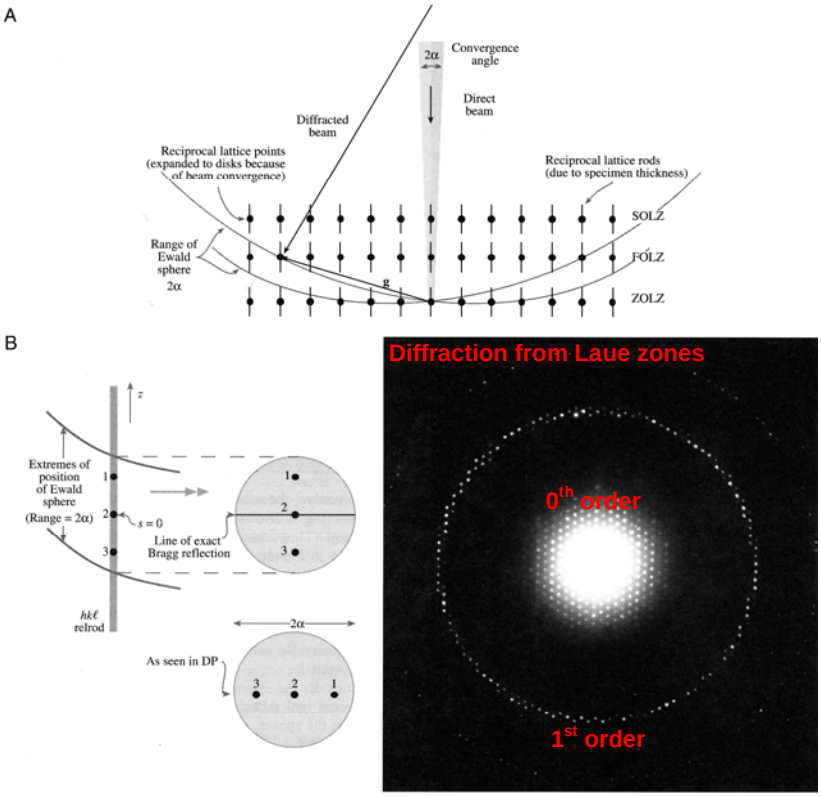

Figure 20.7. (A) The Ewald sphere can intercept reciprocal lattice points from planes not parallel to the electron beam whose **g** vectors are not normal to the beam. The sphere has an effective thickness of 2α because of beam convergence and so intercepts a range of these HOLZ reciprocal lattice points. The relrod has a shape shown in (B) and the intensity at specific points x_i in the relrod is directly related to equivalent points in the *hkℓ* disk. The interception of the Ewald sphere with the HOLZ layers gives rings: the first ring is called the FOLZ, the second the SOLZ, and so on, shown experimentally in (C).

1.5.3 The Intensity of the Diffraction Spots

The intensity of the diffraction spots is given by the structure amplitude: where the scattering amplitudes from all atoms within each unit cells are added up with the appropriate phases.f_i are the atomic form factors, x_i, y_i, and z_i are the coordinates of the i[th] atom, *h,k,l* are the Bragg indices .

$$F_{hk\ell} = \sum_i f_i e^{2\pi i\left(hx_i + ky_i + \ell z_i\right)}$$

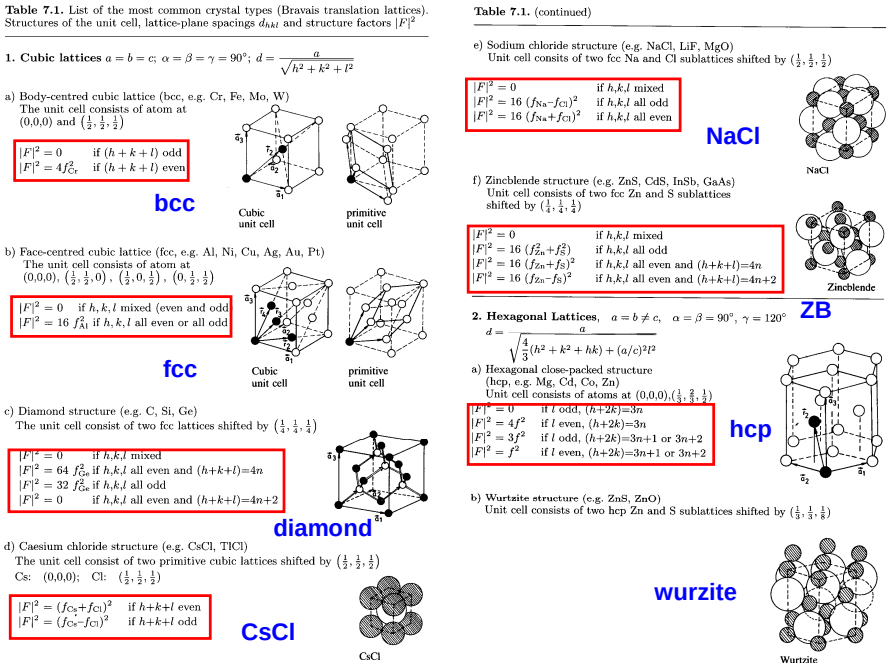

Thus, not all possible reflections appear in the diffraction patterns !

However, because of the very strong electron-sample interaction, multiple scattering effects must be considered for structural analysis.

This requires the application of **dynamical scattering theory**.

1.5.4 Construction of TEM Diffraction Patterns

Recipe: Construct the cross sectional plane in the reciprocal lattice perpendicular to the incident electron beam using: $[hkl] \cdot g^* = 0$ ***Example fcc-lattice*:**

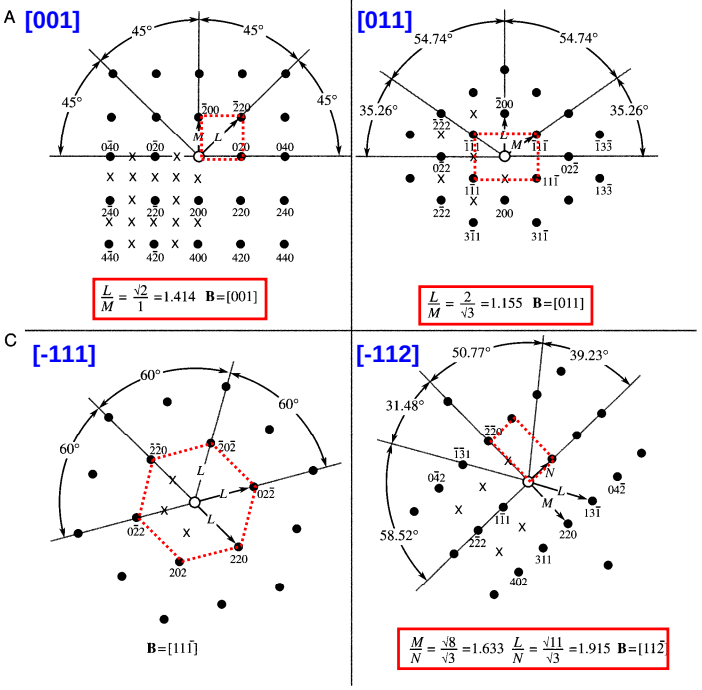

Figure 18.18. Four standard indexed diffraction patterns for fcc crystals in the [001], [011], [$\bar{1}$11], and [$\bar{1}$12] beam directions. Ratios of the principal spot spacings are shown as well as the angles between the principal plane normals. Forbidden reflections are indicated by x.

Example: case [011]:

- shortest perpendicular reciprocal lattice vectors: [100] and [0-11]
- these form the *basis vectors* of the reciprocal lattice plane normal to the [011] electron beam.
- [100] and [0-11] are perpendicular to each other and |0-11| = √2 * |100|.
- Thus, the 2D reciprocal lattice plane consists of a 2D rectangular lattice.
- However, due to the structure factor not all reciprocal lattice points are actually present but only those with F >0.
- For *fcc* lattices. These are all rec. lattice points with all even or all odd indices, i.e., [200], [11-1], [2-22], etc. but not [100] or [0-11]

… Construction of TEM diffraction patterns ….

Recipe: Construct the cross sectional plane in the reciprocal lattice perpendicular to the incident electron beam using: $[hkl] \cdot g^* = 0$ ***Example fcc-lattice*:**

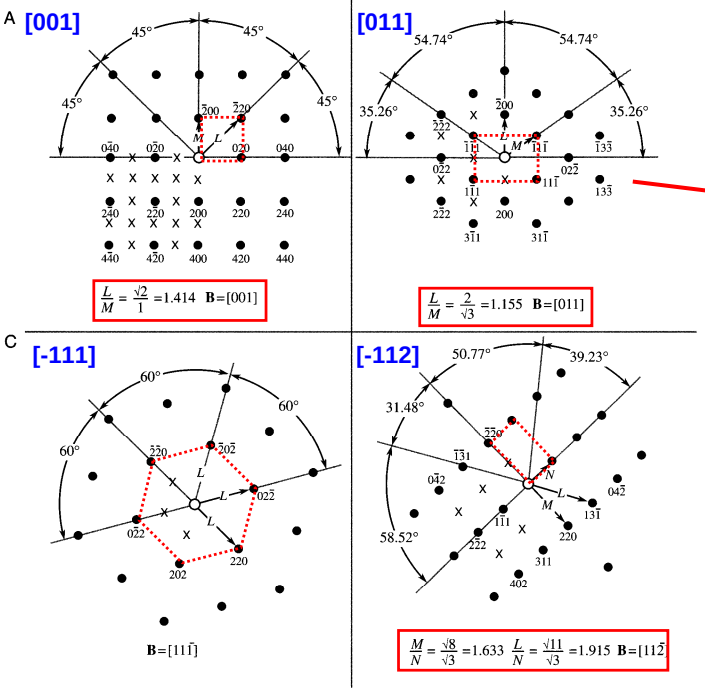

Figure 18.18. Four standard indexed diffraction patterns for fcc crystals in the [001], [011], [$\bar{1}$11], and [$\bar{1}$12] beam directions. Ratios of the principal spot spacings are shown as well as the angles between the principal plane normals. Forbidden reflections are indicated by x.

Determination of crystal orientation and structure:

Symmetry of diffraction spots and relative spacing of nearest and second nearest spot spacing *L*/*M*.

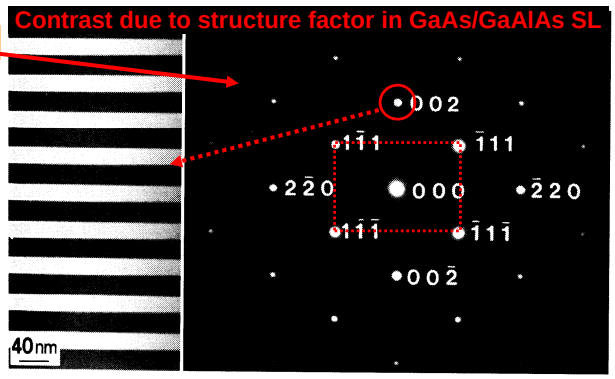

Figure 16.6. (A) DF image from a 002 superlattice reflection in GaAs. The $Al_yGa_{1-y}As$ is the lighter region because Al has replaced Ga in the GaAs (darker regions). (B) Diffraction pattern showing the less intense 002 and other superlattice reflections.

$F_{GaAs}(002) \sim 16(f_{Ga} - f_{As}) \sim 0$
$F_{AlAs}(002) \sim 16(f_{Ga} - f_{Al}) > 0$

1.5.5 Structure Analysis using TEM

Because the electron diffraction pattern represents only one cross section of the reciprocal lattice, more that one diffraction pattern must be recorded for a complete structural analysis.

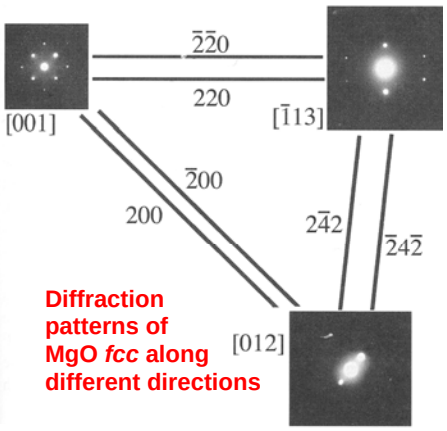

Diffraction patterns of MgO *fcc* along different directions

Example Cu crystal:

Four different zone axis diffraction patterns and corresponding bright fie of a small grain in a Cu foil. The regions marked by 1, 2 and 3 corresp areas used to obtain the diffraction patterns.

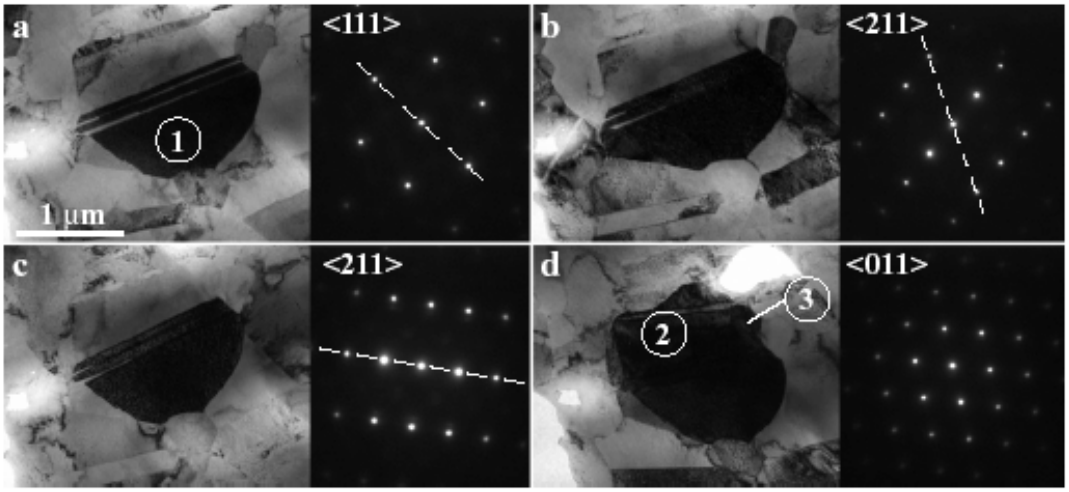

ıtration of the procedure described in Fig his case MgO.

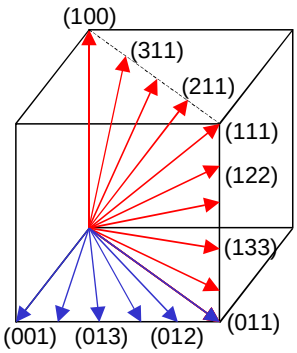

Example Cu crystal:

Comparison of the diffraction pattern with expected patterns for *fcc* lattice:

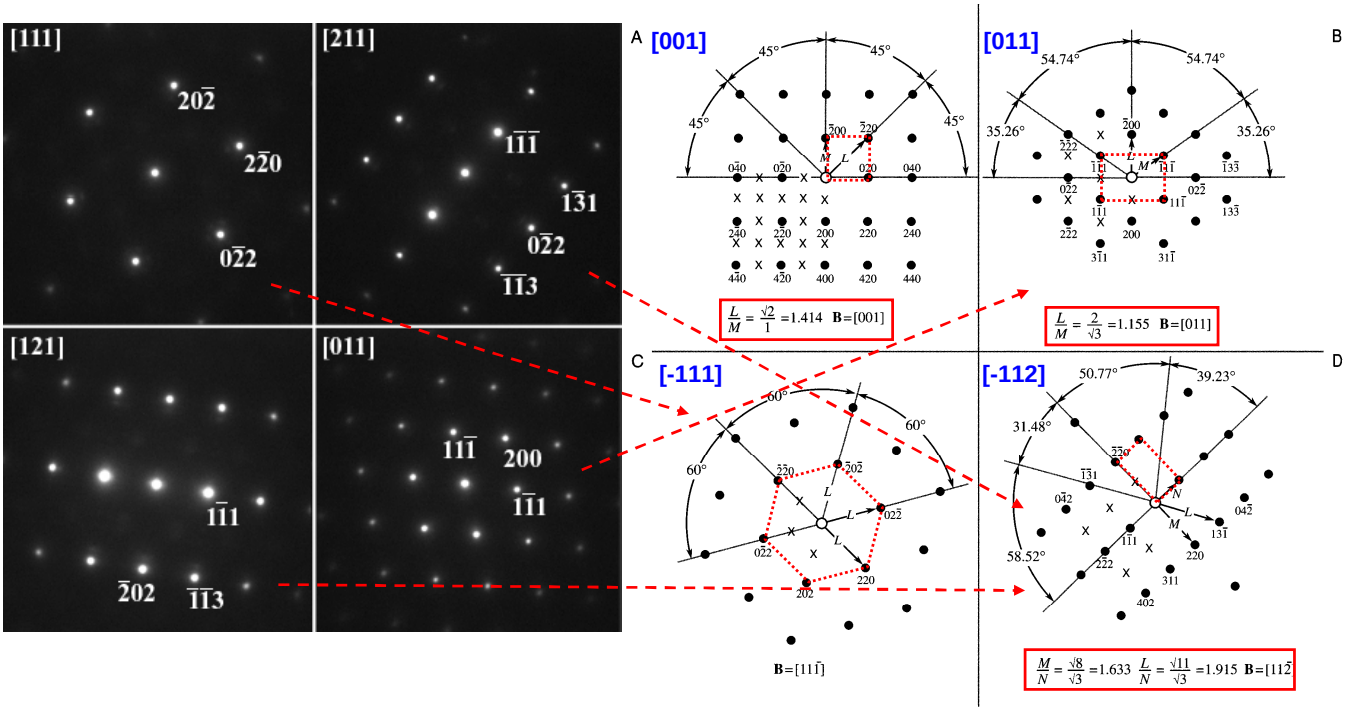

Figure 18.18. Four standard indexed diffraction patterns for fcc crystals in the [001], [011], [$\bar{1}$11], and [$\bar{1}$12] beam directions. Ratios of the principal spot spacings are shown as well as the angles between the principal plane normals. Forbidden reflections are indicated by x.

1.5.6 Polycrystalline Samples

Reciprocal lattice points are converted into reciprocal lattice rings or spheres due the variable orientation of the crystal grains with respect to the electron beam. The cross section of the Ewald sphere or *plane* with these rings yields concentric ring-shaped diffraction patterns (Debeye Scherrer rings).

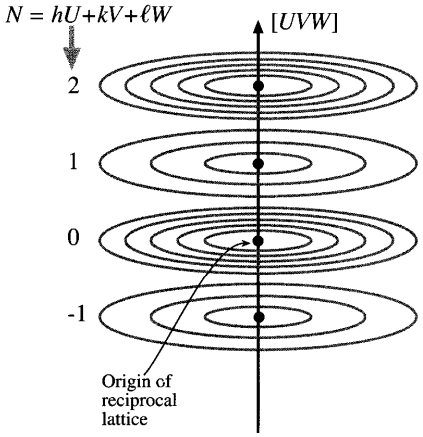

Figure 18.8. The generation of a set of circles in reciprocal space by a textured polycrystal. When the reciprocal lattice is rotated about a particular direction [*UVW*] (in this case the normal to the texture plane), each Laue zone (*N* = 1, 2, etc.) produces a set of concentric circles for each allowed reflection in each zone.

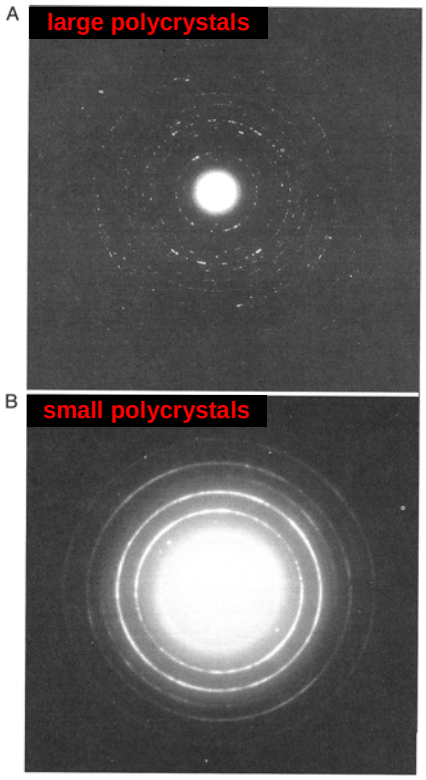

Figure 18.9. Ring diffraction patterns from polycrystalline foils. In (A) the grain size is larger than in (B), so the rings are made up of discrete spots. A finer grain size, as in (B), produces a more continuous ring pattern, but the widths of the rings of diffracted intensity in fact become broader and can be used as an inverse measure of the grain size.

Textured samples

Grains are oriented preferably along certain directions or rotated preferentially around a certain texture axis (fibre axis). When the electron beam parallel to the [mno] fibre axis, again concentric rings are observed. However, in this case not all Debeye-Scherrer rings appear but only those with (hkl) perpendicular to the electron beam, i.e., those with (hkl)[mno]=0.

When the electron beam is inclined to the rotational fibre axis of the crystal grains, the continuous Debeye-Scherrer rings will disrupt into ring segments (see above schematic picture (b) and diffraction pattern (c) right side below).

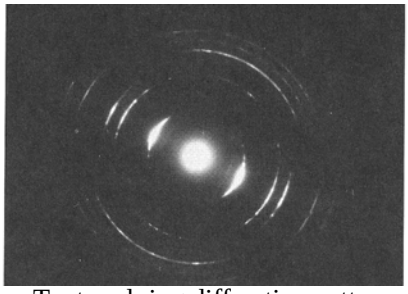

Textured ring diffraction pattern

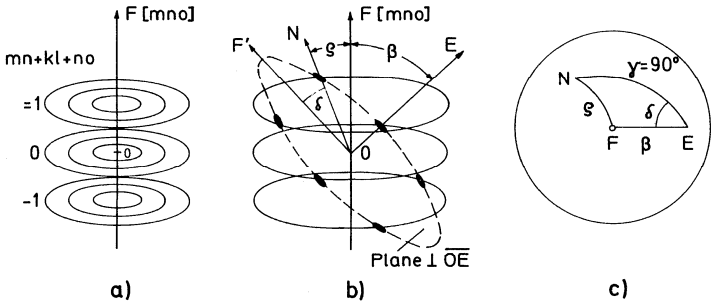

Fig. 8.10. (**a**) Distribution of the g vectors of the crystallites in reciprocal space for foils with a fibre texture with [*mno*] as fibre axis. (**b**) intersection of the Ewald sphere (– – –) with these rings resulting in sickle-shaped segments of the Debye–Scherrer rings. (**c**) Relations between the angles (E: electron-beam direction, N:

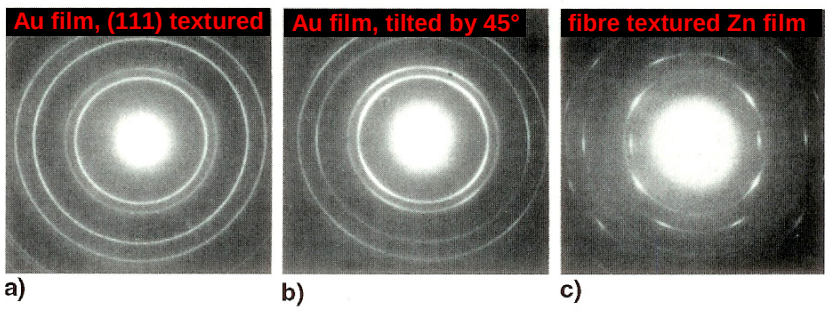

Fig. 8.11. (**a**) Electron diffraction pattern at normal incidence of an evaporated Au film with a weak (111) fibre texture, (**b**) the same specimen tilted 45° to the electron beam showing a weak dependence of the ring intensities on the azimuth. (**c**) Strong fibre texture of an evaporated Zn film tilted at 45° to the electron beam

1.5.7 Other Examples:

Superlattices and phase analysis

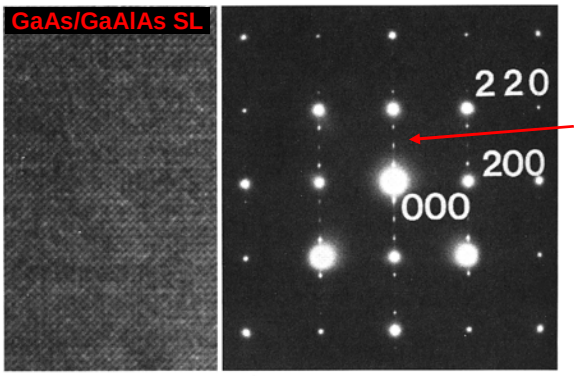

Figure 16.8. (A) Artificial GaAs/$Al_xGa_{1-x}As$ structure in which order is created by alternating four layers of GaAs and four of $(Al_xGa_{1-x})As$.

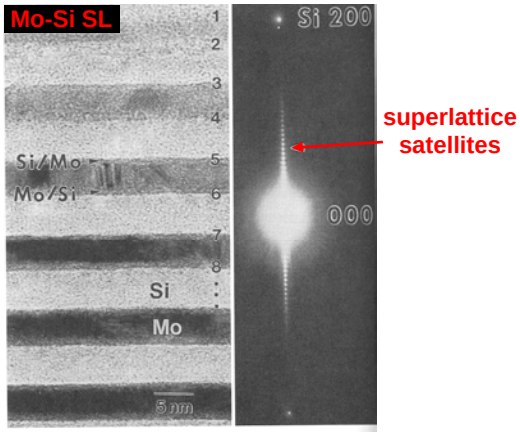

Figure 16.9. (A) Artificial superlattice of Si and Mo layers ~5 nm thick (B) Expanded DP around 000 showing many superlattice spots (ar-

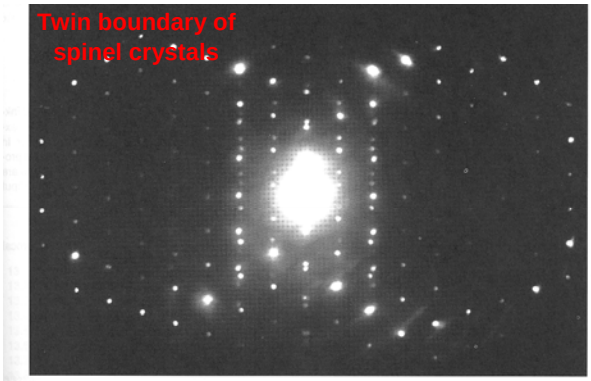

Figure 12.7. Diffraction pattern taken across a twin boundary in $MgAl_2O_4$ spinel. The rings of bright spots show where the Ewald sphere intercepts the reciprocal lattice of the crystals either side of the twin boundary.

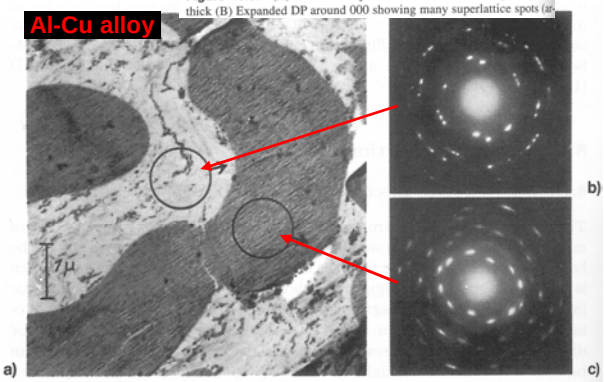

Fig. 8.1a–c. Example of a selected-area electron diffraction (SAED) from a thin section of an Al-Cu eutectic cut with a microtome. (**b**) (Al matrix) and (**c**) ($AlCu_2$) contain the SAED pattern of the circles indicated in (**a**)

Diffraction patterns from twinned Cu grains along [110] zone axis:

Superposition of three [110] diffraction patterns mirrored with respect to each other

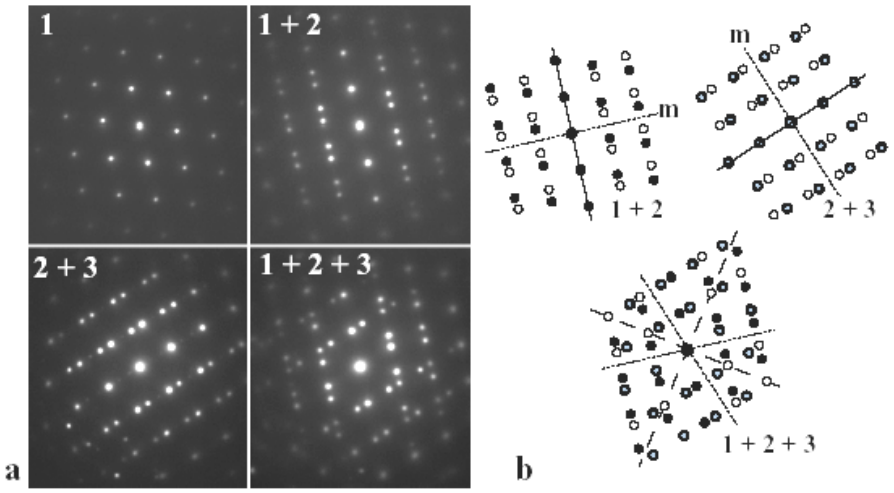

Fig. 9.4. Zone axis diffraction patterns of twins in the Cu grains shown in Fig. 4.21. The experimental patterns across several twin boundaries (a) are shown as simulated patterns in (b).

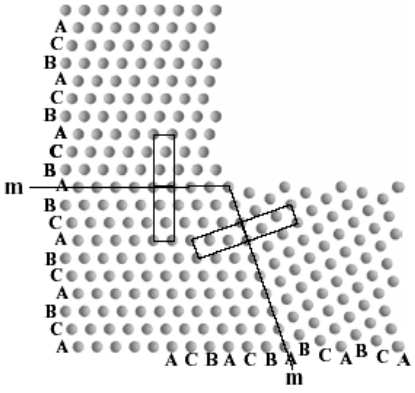

Schematic illustration of mirror twin boundaries in a fcc cubic lattice. The twin planes mirror the ABC stacking sequence into the CBA sequence.

Different diffraction patterns obtained by moving the electron beam across the twin boundaries.

1.6 Contrast Mechanisms in TEM

1.6.1 Mass-Thickness Contrast

Electron scattering within the sample leads to **(a) Loss of electron energy.**
(b) Deflection away from the optical axis.

Both processes strongly depend on the **sample thickness** as well as **atom mass** and **Z number**:

- ❖ Heavier elements scatter electrons more strongly than light elements.
- ❖ Scattering loss increases with sample thickness.

Deflection away from optical axis through elastic scattering:

$$\sigma_{el}(\theta > \alpha_0) \approx \frac{Z^{4/3}\lambda^4(1+E/E_0)^2}{\pi\lambda^2 + \pi(2\alpha_0 a_B)^2 Z^{-2/3}}$$

⇨ Strongly deflected electrons with $\theta > \alpha_0$ are blocked by the objective aperture, i.e., the stronger the scattering the smaller the transmitted electron current !

⇨ Regions with larger sample thickness and/or higher Z number and atom mass appear darker in the TEM image !

⇨ Dominating contrast mechanism for low and medium magnification and small electron transmission, i.e., for thick sample specimen.

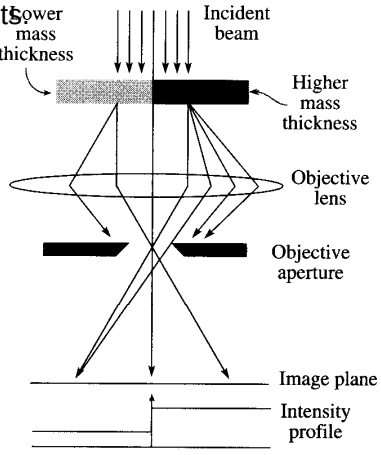

Figure 22.4. Mechanism of mass-thickness contrast in a BF image. Thicker or higher-Z areas of the specimen (darker) will scatter more electrons off axis than thinner or lower-mass (lighter) areas. Thus fewer electrons from the darker region fall on the equivalent area of the image plane (and subsequently the screen), which therefore appears darker in BF images.

Example for Z-contrast: Transistor cross sections (Z-numbers: Si=16, N=7, O=8, Cu=29)

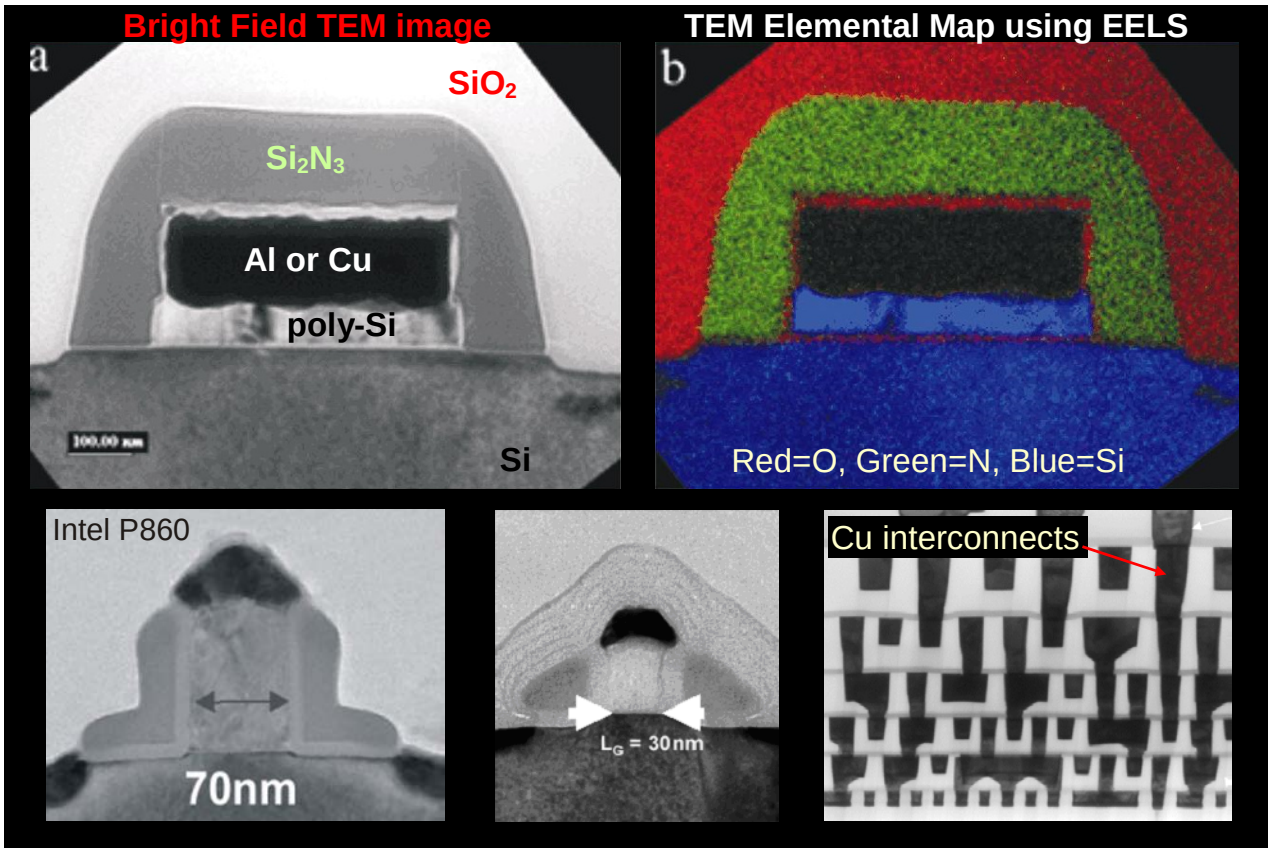

Local electron intensity: Given by the transmission probability of the electrons through the aperture α_0:

$$T(\alpha_0, E_0, \rho \cdot d) = j / j_0 = \exp(-\rho \cdot d / \kappa)$$

where κ is the characteristic contrast thickness characteristic for each element and the used aperture angle as well as electron energy.
It can be viewed as an absorption coefficient.

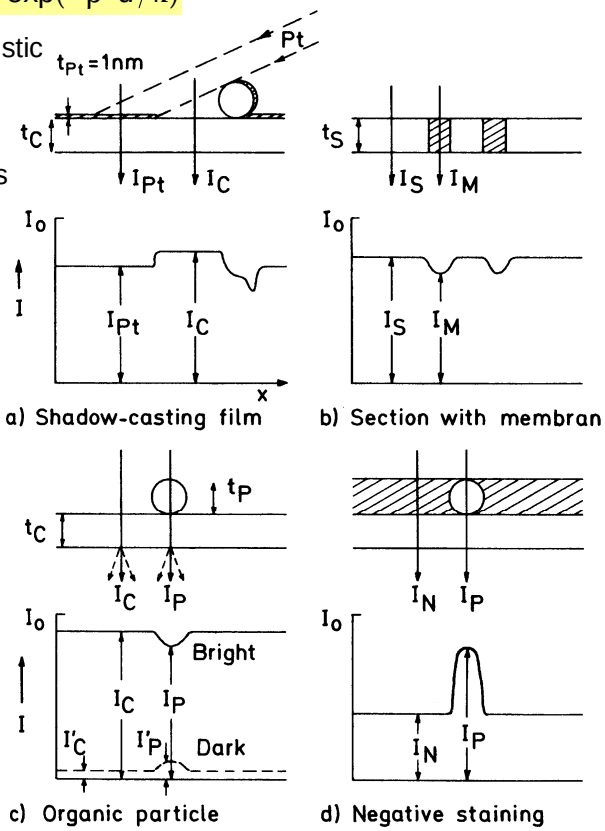

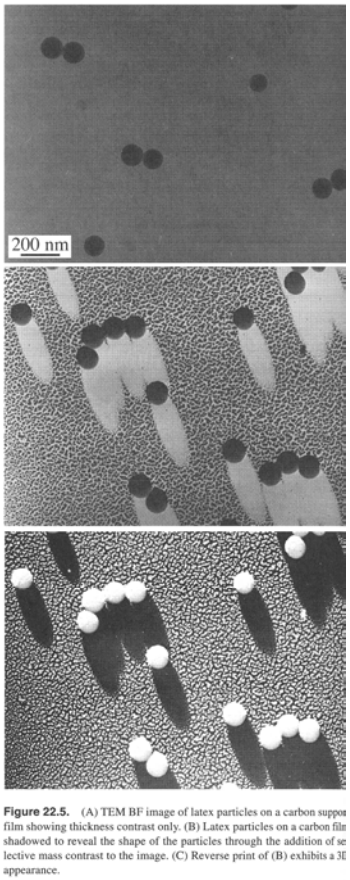

Figure 22.5. (A) TEM BF image of latex particles on a carbon suppor film showing thickness contrast only. (B) Latex particles on a carbon filr shadowed to reveal the shape of the particles through the addition of se lective mass contrast to the image. (C) Reverse print of (B) exhibits a 3I appearance.

Examples:

Further examples:

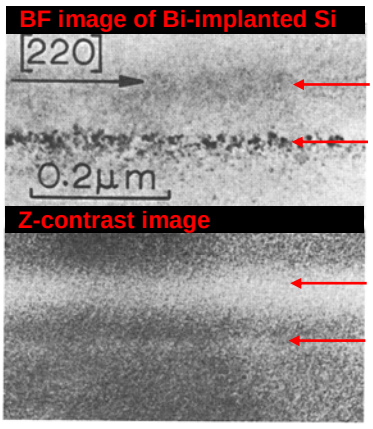

Figure 22.14. (A) Low-resolution TEM BF image showing a row of defects in Bi-implanted Si. In (B), obtained under Z-contrast conditions, the defects associated with the implant are invisible but the specimen is bright in the region implanted with Bi.

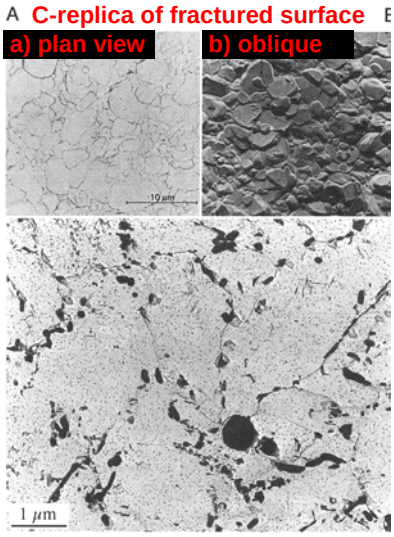

Figure 22.11. More examples of mass-thickness contrast: (A) a carbor replica of a fracture surface doesn't show much of either form of contras until (B) oblique shadowing enhances the topography. (C) An extractior replica of a range of small precipitate particles in a Cr-Mo steel wele shows both mass and thickness contrast.

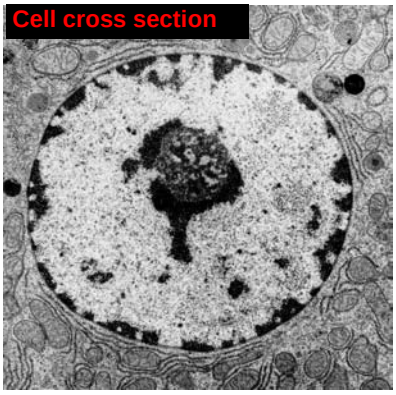

- Mass-thickness contrast is most important for amorphous and organic samples.
- The mass-thickness contrast is opposite as for SEM: Areas with heavier elements appear darker in the TEM image due to the increased scattering loss.

How can the mass thickness contrast be increased ?

(a) Using lower electron energies and smaller objective apertures α.
(b) By energy filtering of the transmitted beam.

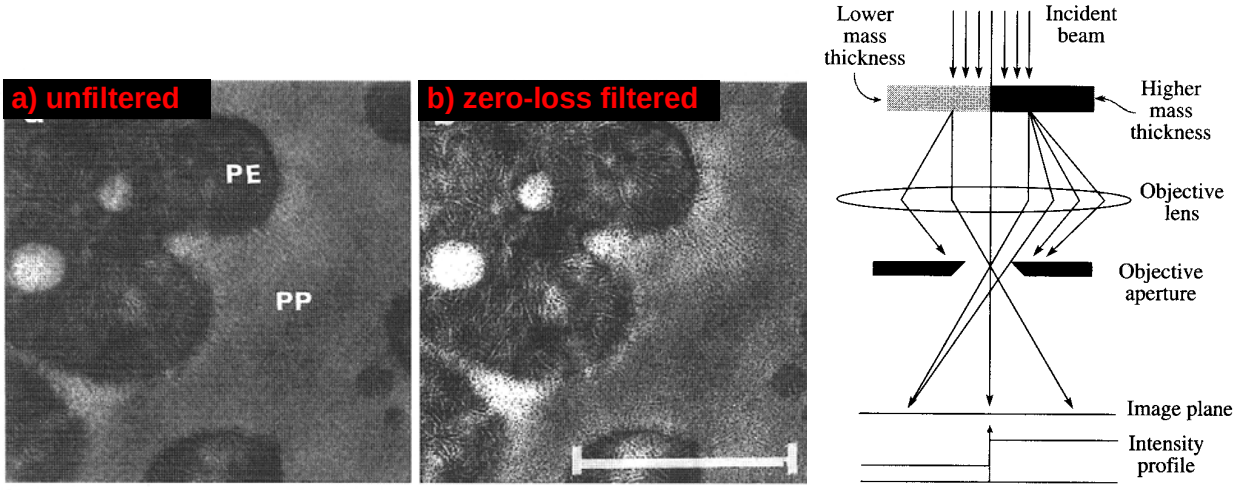

Fig. 6.7. Comparison of (**a**) an unfiltered and (**b**) zero-loss filtered image of a thin section of a copolymer of polyethylene (PE) and polypropylene (PP) stained with ruthenium oxide ($E = 80$ keV, bar $= 0.5$ μm)

1.6.2 Diffraction and Strain Contrast in TEM

Diffraction contrast can be obtained in the ***bright-field*** as well as ***dark-field mode***.
In these cases, **only a selected part** of the diffraction pattern is used for image formation.

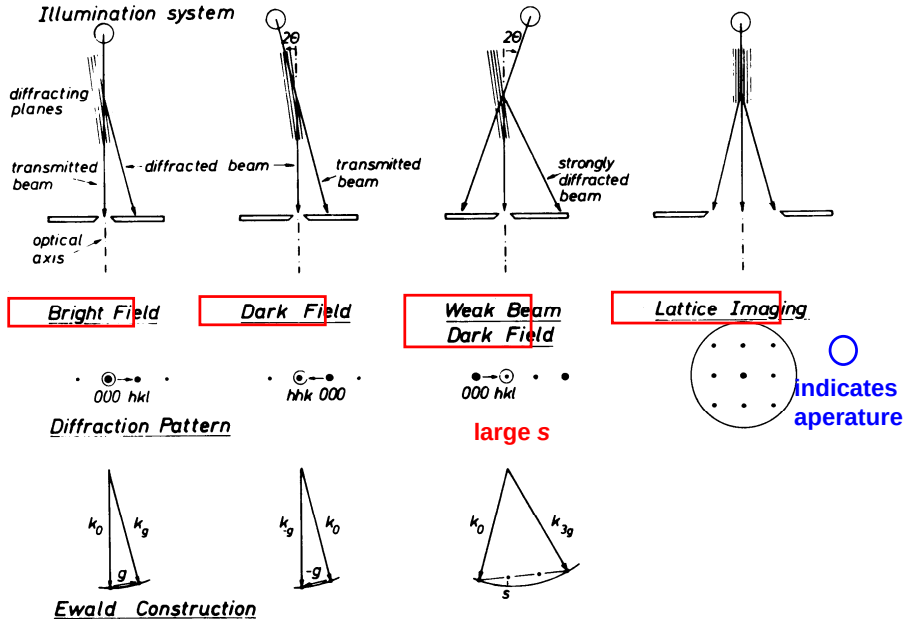

Fig. 2. Ray diagrams (including Ewald sphere construction) for: (a) a conventional two-beam bright-field (BF) image; (b) dark-field (DF) image; (c) weak-beam dark-field (WBDF) image; (d) lattice image. The gun of the electron microscope is tilted by the appropriate angle in going from (a) to (b) or from (a) to (c).

Diffraction contrast: Whenever diffraction effects from a local sample areas cause a change in the intensity distribution among the diffraction spots, the corresponding intensity in the TEM image will change.

Thus, the TEM image will show diffraction contrast.

This contrast is usually stronger in the dark-field mode.

Example: (002) dark-field image of GaAs/GaAlAs superlattice. Because $F_{(002)} \sim f_{As} - f_{Ga/Al}$, the GaAlAs layers appear brighter than the GaAs

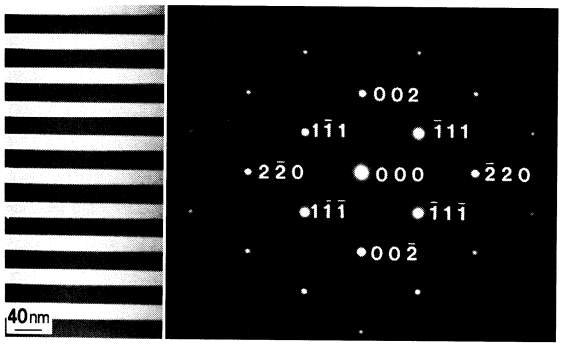

Figure 16.6. (A) DF image from a 002 superlattice reflection in GaAs. The $Al_xGa_{1-x}As$ is the lighter region because Al has replaced Ga in the GaAs (darker regions). (B) Diffraction pattern showing the less intense 002 and other superlattice reflections.

Origin of changes in diffraction intensity:

- Local changes in crystal structure.
- Local changes in structure factor or atomic form factors.
- Local changes and tilts in crystal orientation.
- Local bending of lattice planes and lattice spacings due to inhomogenous strains in the samples caused by: inclusions, dislocations, stacking faults, phase boundaries, and other crystal defects.

Example:

Diffraction contrast in the bright field mode for a thin Ti- foil:

Make dislocations and crysal defects visible in the selected sample area.

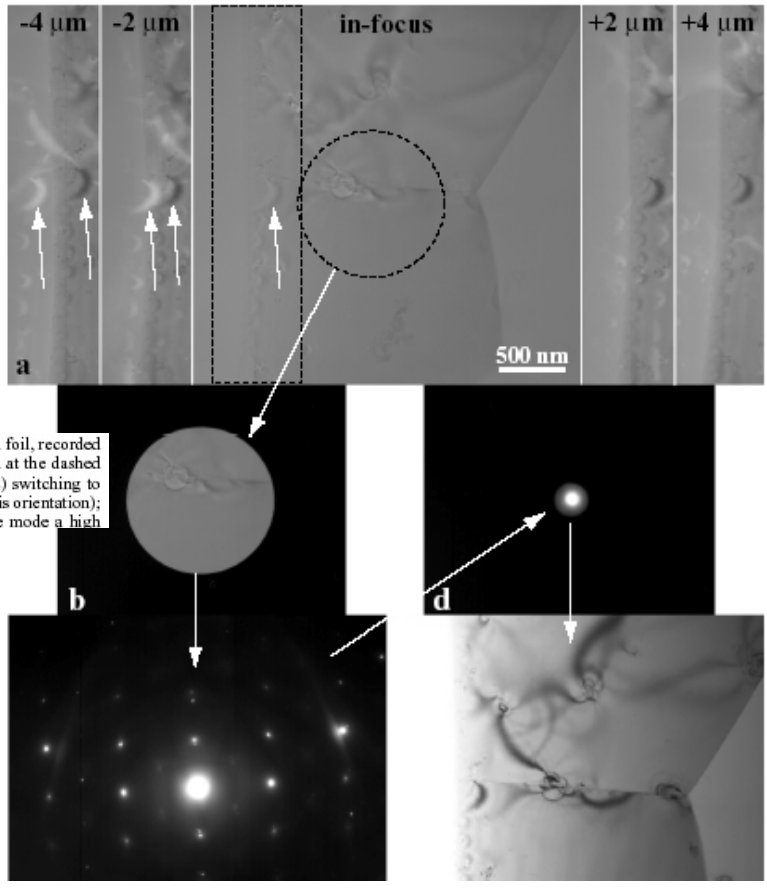

Fig. 4.10. a) experimental illustration of in-focus and out-of-focus images of a Ti foil, recorded with no apertures inserted in the column; b) the selected area aperture is placed at the dashed circle in the center image of a), and the image inside the aperture is focused; c) switching to diffraction mode, a diffraction pattern is obtained (in this case near [01.0] zone axis orientation); d) the diffraction aperture is inserted around the central beam, and e) in image mode a high

Two-beam mode: to enhance the diffraction contrast, in the two beam mode the sample is tilted in such a way that the intensity of one particular diffraction spot is maximized.

Example: Al-Li alloy layer with Al_3Li precipitates

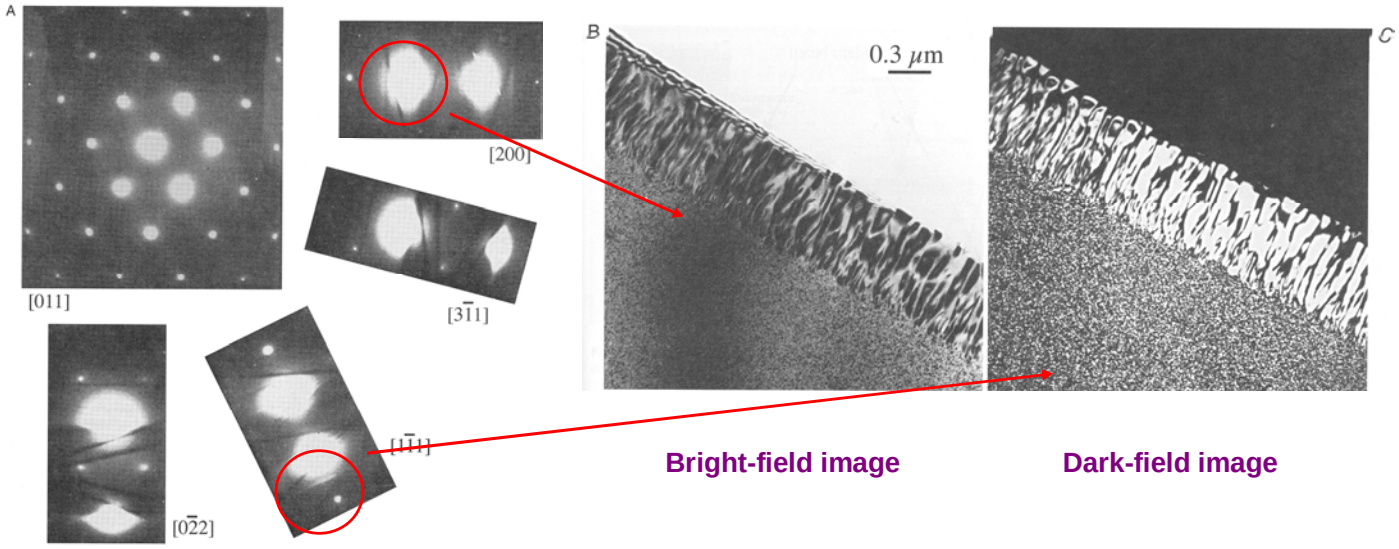

Figure 22.16. (A) The [011] zone-axis diffraction pattern has many planes diffracting with equal strength. In the smaller patterns, the specimen is tilted so there are only two strong beams, the direct 000 on-axis beam and a different one of the $hk\ell$ off-axis diffracted beams. Complementary (B) BF and (C) DF images of Al-3 wt.% Li taken under two-beam conditions are shown also. In (B) the Al_3Li precipitate phase (present as tiny spheres in the grain and coarse lamellae at the boundary) is diffracting strongly and appears dark. In (C), imaged with a precipitate spot, only the diffracting precipitates appear bright.

1.6.3 Contrast due to Strain Fields caused by Dislocations and Inclusions

Dislocations: Are line defects in the crystal, which are characterized by the dislocation Burgers vector ***b*** as well as the dislocation line direction ***u***.

The dislocation Burgers vector can be obtained from the **Burgers circuit**. Depending on the angle between ***b*** and ***u***, the dislocation can have either a **screw, and edge or a mixed character**.

For **pure edge dislocations**, the dislocation corresponds to an additional inserted or removed lattice plane. In this case, ***b*** is normal to this lattice plane and its length is equal to the corresponding lattice plane spacing.

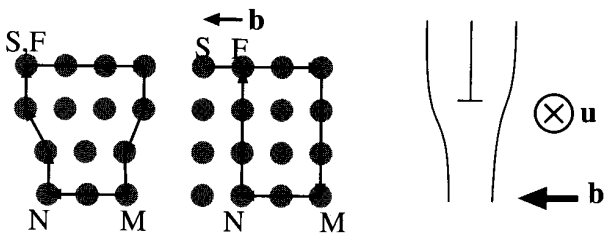

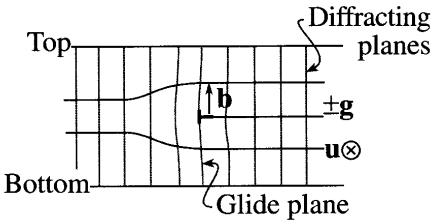

Figure 25.4. Buckling of the glide planes arises because of the term **g**·**b**×**u** and is important because it complicates the analysis of **b**.

- Bending of lattice planes & local change in lattice spacing.

For **pure screw dislocations**, ***b*** is parallel to ***u***.

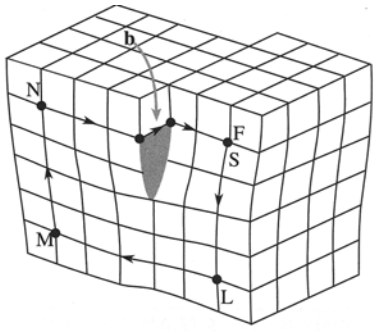

- Only bending of lattice planes but no change of lattice spacing.

Dislocations cause **a local bending of the crystal lattice planes** and thus to local variations of the Bragg diffraction angles. Thus, diffraction contrast can be utilized to make the dislocations visible in the TEM images.

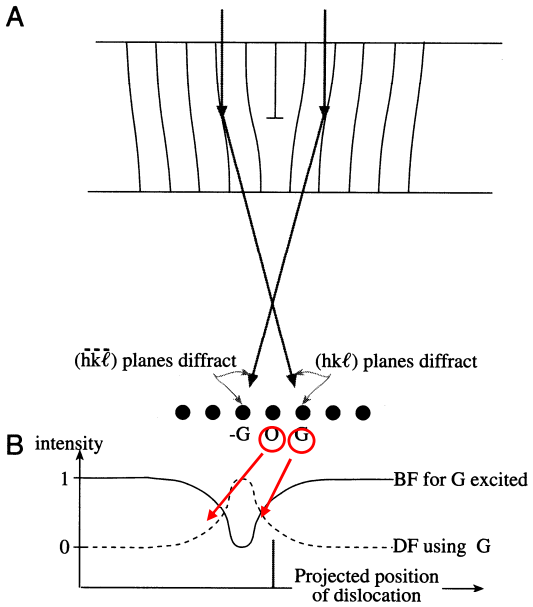

Figure 25.1. (A) The specimen is tilted slightly away from the Bragg condition ($\mathbf{s} \neq 0$). The distorted planes close to the edge dislocation are bent back into the Bragg-diffracting condition ($\mathbf{s} = 0$), diffracting into G and –G as shown. (B) Schematic profiles across the dislocation image showing that the defect contrast is displaced from the projected position of the defect.

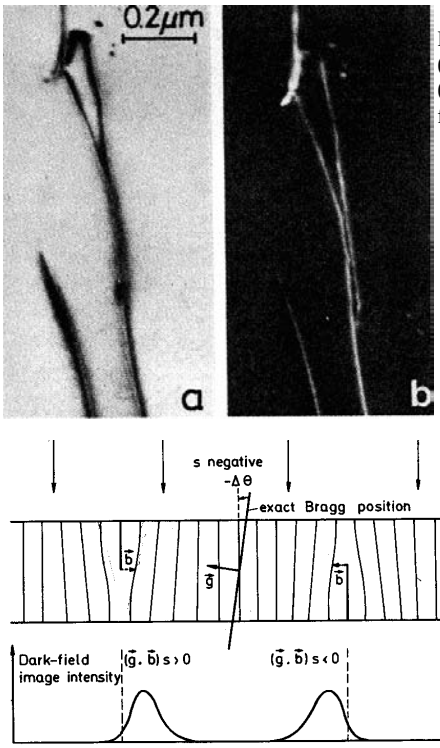

Figure: Dislocations in silicon: (a) strong-beam bright field image, (b) same area imaged under dark-filed weak beam conditions.

Fig. 9.21. Diagram showing on which side of its core the dislocation image is situated

➢ The image of the dislocation is always laterally displaced from the real position of the dislocation !

The bending of the crystal lattice plane is related to the **distortions of the crystal lattice** around the dislocations. In elastically isotropic solids these are described by the displacement field R(x,y,z) = R(r,ϕ):

$$\mathbf{R} = \frac{1}{2\pi}\left(\mathbf{b}\phi + \frac{1}{4(1-\nu)}\left\{\mathbf{b}_e + \mathbf{b}\times\mathbf{u}\left(2(1-2\nu)\ln r + \cos 2\phi\right)\right\}\right)$$

(for a general mixed dislocation)

$$\mathbf{R} = \mathbf{b}\frac{\phi}{2\pi} = \frac{\mathbf{b}}{2\pi}\tan^{-1}\left(\frac{z-z_d}{x}\right)$$

(for a pure screw dislocation)

where $\mathbf{b}_e$ is the edge component of **b** , and ν is the Poisson ratio of the material.

In particular, mainly those crystal lattice planes are strong bend that are normal to the displacements **R**.

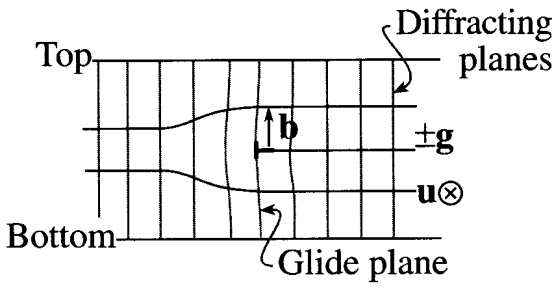

Figure 25.4. Buckling of the glide planes arises because of the term $\mathbf{g}\cdot\mathbf{b}\times\mathbf{u}$ and is important because it complicates the analysis of **b**.

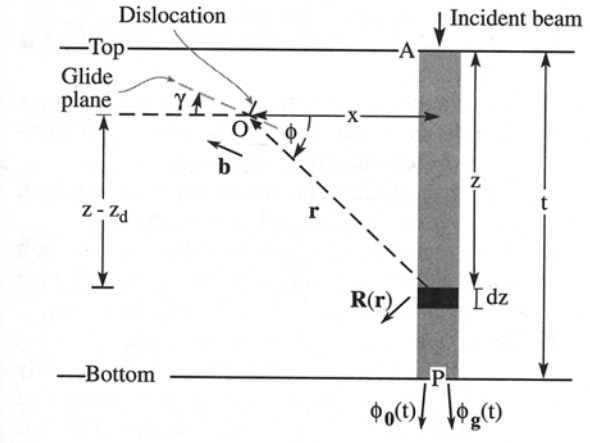

Figure 25.3. The effect of a dislocation with Burgers vector, **b**, at O on a column, distance *x* away. The effect of the strain field on the electron waves in the column is integrated in increments *dz* over its total length *t*, giving amplitudes $\phi_0(t)$ and $\phi_g(t)$ at P.

The lattice distortions are proportional to ***R*** and the bending perpendicular to ***R***:

Visibility condition for dislocations: **$(g \cdot R) > 0$**

(i) **Screw dislocations**: ***R ~ b***: dislocations invisible when **$(g \cdot b) = 0$**

(ii) **Edge dislocations**: ***R ~ b + b × u***:
dislocations invisible when **$(g \cdot b) = 0$** and $(g \cdot b \times u) < 0.64$

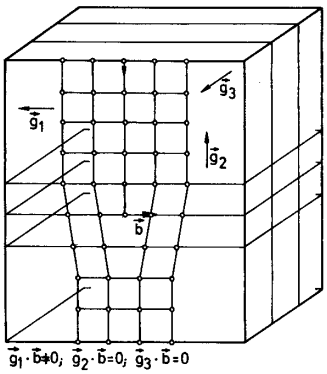

Edge dislocations:

Fig. 9.23. Demonstration of the $g \cdot b = 0$ rule for an edge dislocation. Only the lattice planes that belong to g_1 are strongly bent, so that $g_1 \cdot b \neq 0$ whereas $g_2 \cdot b = g_3 \cdot b = 0$

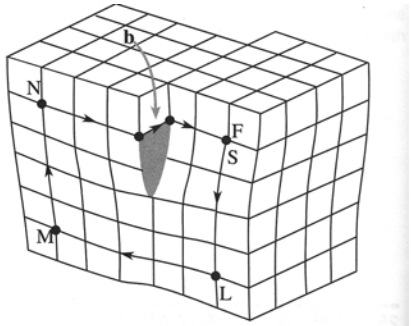

Screw dislocations:

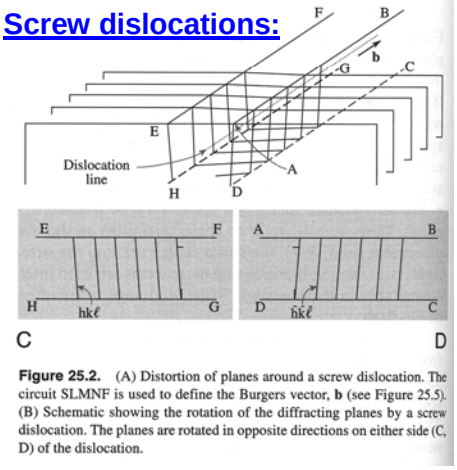

Figure 25.2. (A) Distortion of planes around a screw dislocation. The circuit SLMNF is used to define the Burgers vector, **b** (see Figure 25.5). (B) Schematic showing the rotation of the diffracting planes by a screw dislocation. The planes are rotated in opposite directions on either side (C, D) of the dislocation.

- The dislocation Burgers vector can be determined by finding two directions g_1 and g_2 in which the dislocation is invisible in the TEM image.

In the TEM images the dislocations appear laterally displaced from their real position in the crystal and they are substantially broadened in proportion to the distance ***s*** of the diffraction spot from the Ewald sphere.

This broadening is particularly large under two-beam conditions where ***s*** ~ 0.

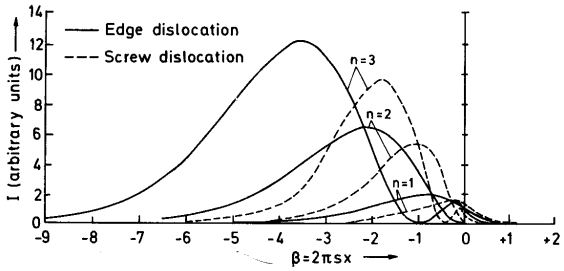

Fig. 9.20. Intensity profiles proportional to $\overline{AB}^2$ in Fig. 9.19 across the dark-field images of edge and screw dislocations with different values of $g \cdot b = n$. The centre of the dislocation is at $x = 0$ [9.50]

This can be drastically reduced by using the

Weak-beam dark field mode.

In this mode, the sample is tilted such that the diffraction spots become rather weak, thus increasing the excitation error ***s***. This strongly reduces the effective width of the dislocations in the TEM images, although the overall intensity is also drastically reduced.
The width of dislocations in the TEM images can be reduced from 5-20 nm to 1.5 – 2 nm.

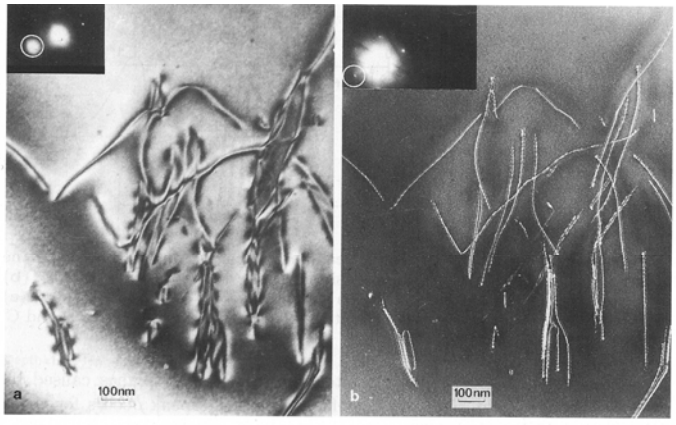

Fig. 9.24. (a) Dislocations in heavily deformed silicon imaged with a strong $2\bar{2}0$ diffracted beam. (b) Weak-beam $2\bar{2}0$ dark-field image of the same area showing the increase of the resolution of dislocation detail. The insets show the diffraction conditions used to form the images [9.91]

Additional examples of dislocation images

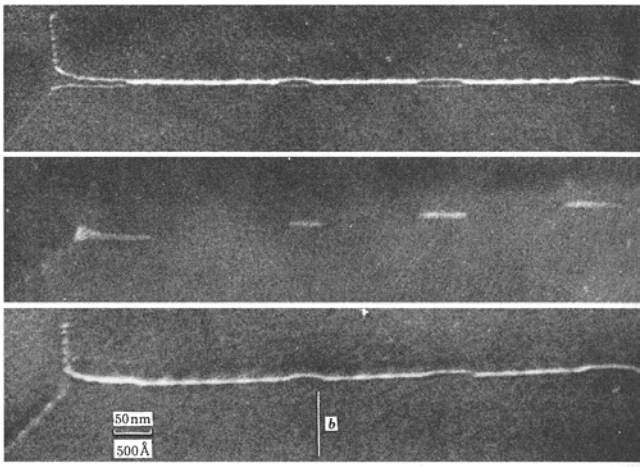

Figure 26.18. WB image of a dislocation in Si which has both dissociated and constricted segments: (A) $\mathbf{g}\cdot\mathbf{b} = 2$; both partial dislocations are visible. (B) $\mathbf{g}\cdot\mathbf{b}_T = 0$ showing SF contrast. (C) $\mathbf{g}\cdot\mathbf{b} = 1$; only one partial dislocation is visible.

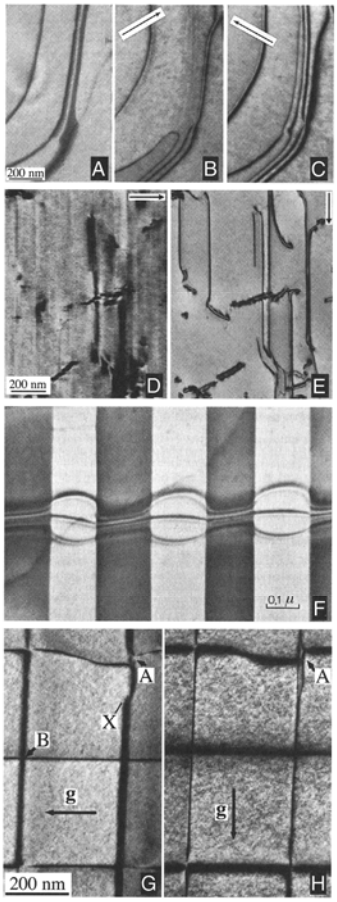

Figure 25.6. (A–C) Three strong-beam BF images from the same area using (A) {11Ī} and (B,C) {220} reflections to image dislocations which lie nearly parallel to the (111) foil surface in a Cu alloy which has a low stacking-fault energy. (D,E) Dislocations in Ni_3Al in a (001) foil imaged in two orthogonal {220} reflections. Most of the dislocations are out of contrast in (D). (F) A complex dislocation crossing a (rotational) domain boundary; the character of the dislocation changes and thus its dissociation width changes. (G,H) Dislocations in a (001) interface between two slightly lattice-mismatched III-V compounds.

Contrast due to strain fields caused by coherent inclusions

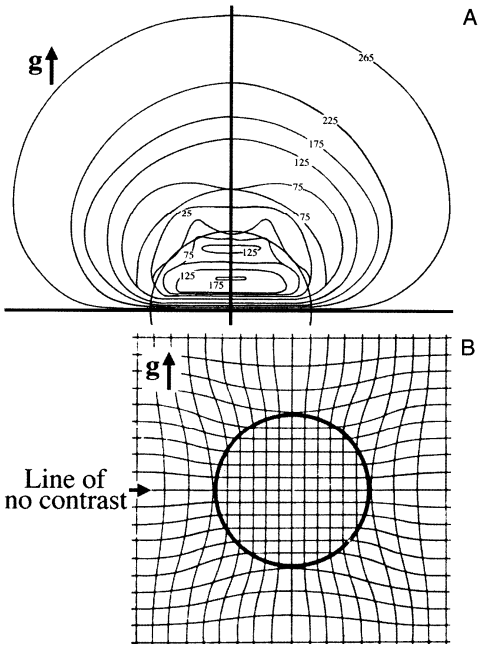

(A) Intensity contours from a simulated image like that shown in (b). Notice the line of no contrast, which corresponds to the plane that is not distorted by the strain field. (C) Experimental image of a coherent particle in Cu-Co showing strain contrast

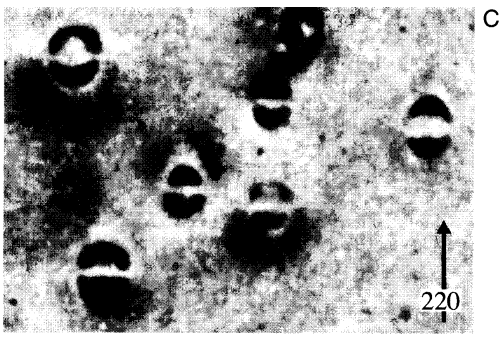

Figure 25.26. (A) Intensity contours from a simulated image of a particle like that shown schematically in (B). Notice the line of no contrast which corresponds to the plane that is not distorted by the strain field of the particle. (C) Experimental image of coherent particles in Cu-Co showing strain contrast.

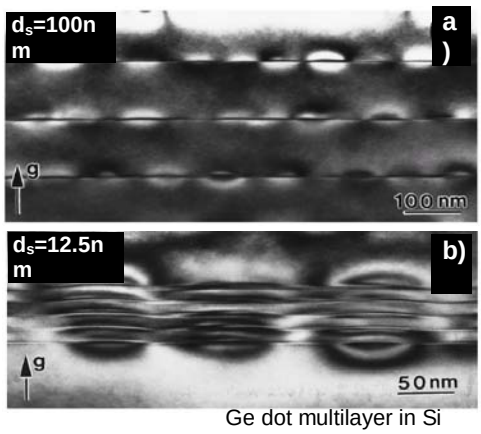

Ge dot multilayer in Si

1.6.4 Phase Contrast

Interference between electrons scattered from different parts of the sample

Result: **Formation of Moire patterns**

TEM image corresponds to summation of information over the whole sample cross-section.
When different lattice periodicities are present along the electron path, a Moiré pattern is formed due to the superposition of two periodic images that are slightly rotated with respect to each other or have a slightly different lattice periodicity.

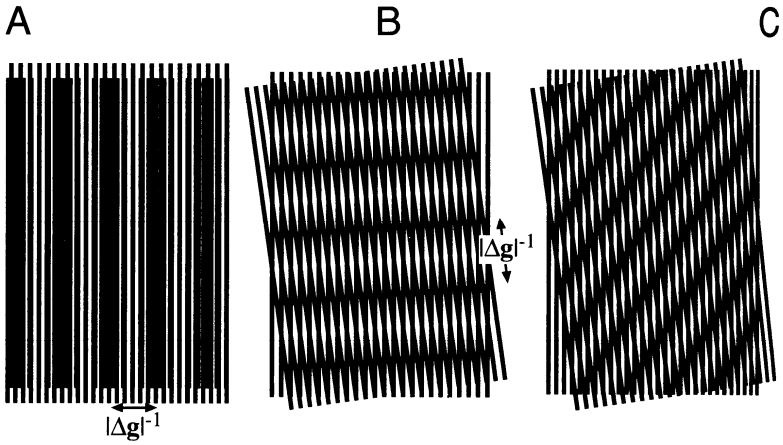

Figure 27.5. (A) Translational moiré fringes; (B) rotational moiré fringes; (C) mixed moiré fringes; note the relationship between the fringes and their constituent lattices.

Examples:

- Samples containing dislocations.
- Contrast at heterointerfaces or phase boundaries.
- Epitaxial layers.
- Inclusions.

Application:

Periodicity of Moiré fringes can be used for determination of the relative differences in the lattice parameter of two materials.

Example: Moiré patterns due to dislocations

Dislocations lead to change in average lattice constant + local deviations from the perfect lattice structure

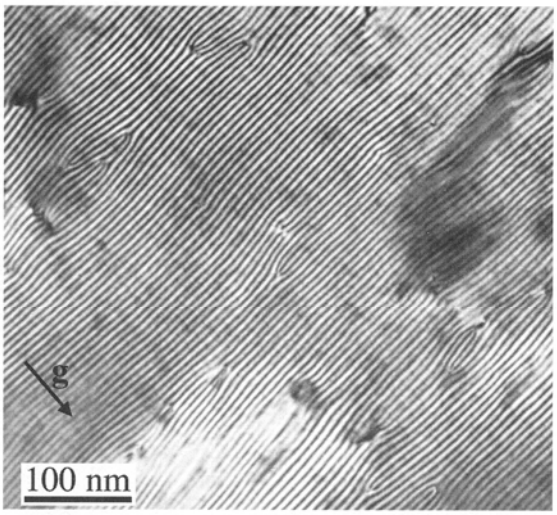

Figure 27.10. Moiré fringes reveal the presence of dislocations in a thin film of CoCa grown on a GaAs substrate. The (001) interface lies parallel to the specimen surface. Although the images contain much detail, most of it cannot readily be related to the structure of the defects.

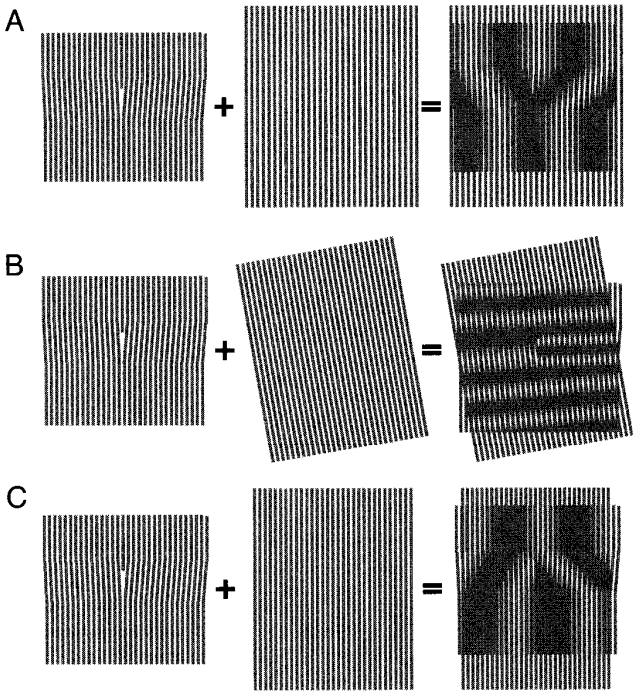

Figure 27.11. Schematic diagrams showing why moiré patterns from regions containing dislocations cannot be readily interpreted: (A) a dislocation image formed by interference between a regular lattice and one containing an extra half plane. (B) In comparison with (A), small rotation of the lattice of either grain can cause a large rotation of the dislocation fringes. (C) A small spacing change of either lattice can cause the dislocation image to reverse.

Moiré patterns due to **superposition of lattices with different lattice constant**

Example: β-SiC precipitates in Si matrix

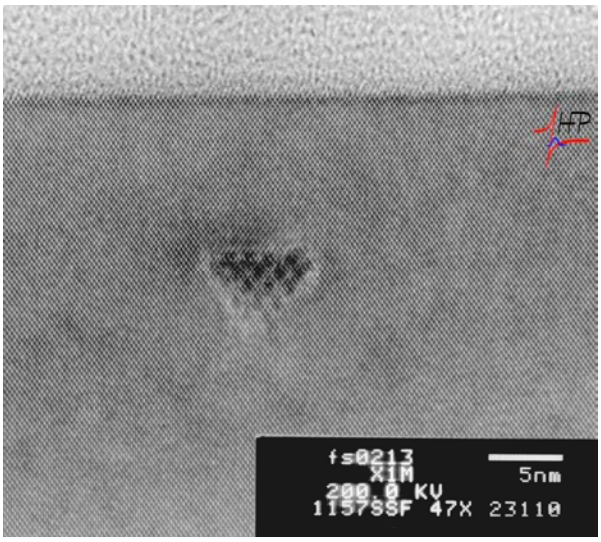

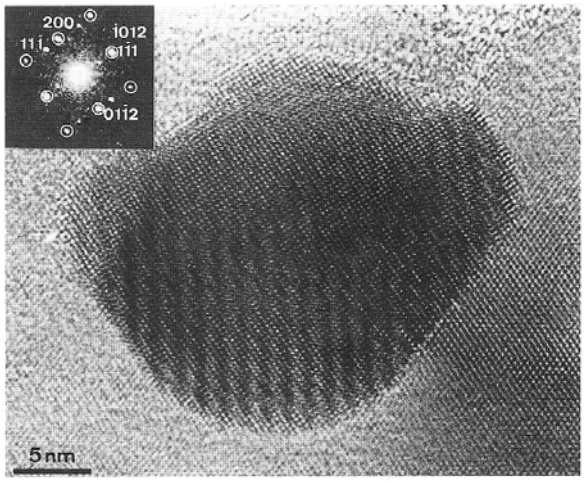

Figure 1-72. One-dimensional moiré pattern between a SiC particle and a silicon matrix superposed on a high-resolution dot pattern (Courtesy De Veirman).

- 19.6 % difference in the lattice constant.
- Moiré periodicity of $p = (a_1 \cdot a_2) / (a_1 - a_2) \approx \langle a \rangle / \Delta a = 5 \cdot \langle a \rangle$.

1.7 High Resolution Lattice Imaging

To get **atomically resolved images**, higher order diffraction spots must be included in the image formation. Modern TEMs allow a resolution of down to 1 Å.

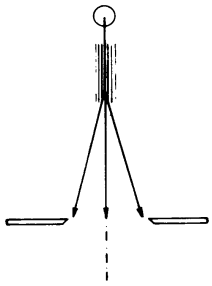

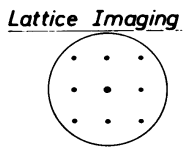

The following requirements must be met for high-resolution TEM imaging:

- ❖ Operation voltages higher than 200 keV.
- ❖ High gun brightness and low energy spread for good temporal coherence.
- ❖ Thin sample specimens.
- ❖ Parallel beam illumination with high spatial coherence (small illumination aperture
- ❖ Optics with small aberration constants (C_s = 0.5 mm or smaller).
- ❖ Precise sample alignment along a low-indexed zone axis.
- ❖ Small sample drifts and vibration free mechanical alignment.

The contrast in the HRTEM images, however, does not directly reflect the atom positions in the crystal lattice.

In particular, the appearance of the HRTEM images depends on many factors such as aperture radius, sample thickness, focus position within the sample, etc.

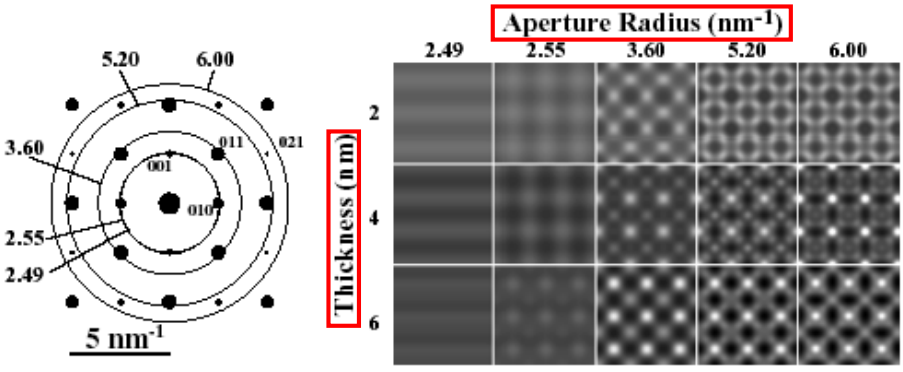

Fig. 10.31. Influence of the aperture size on simulated HREM images, for 5 different aperture sizes indicated on the $BaTiO_3$ [100] zone axis pattern. See text for more details.

Example for HRTEM images:

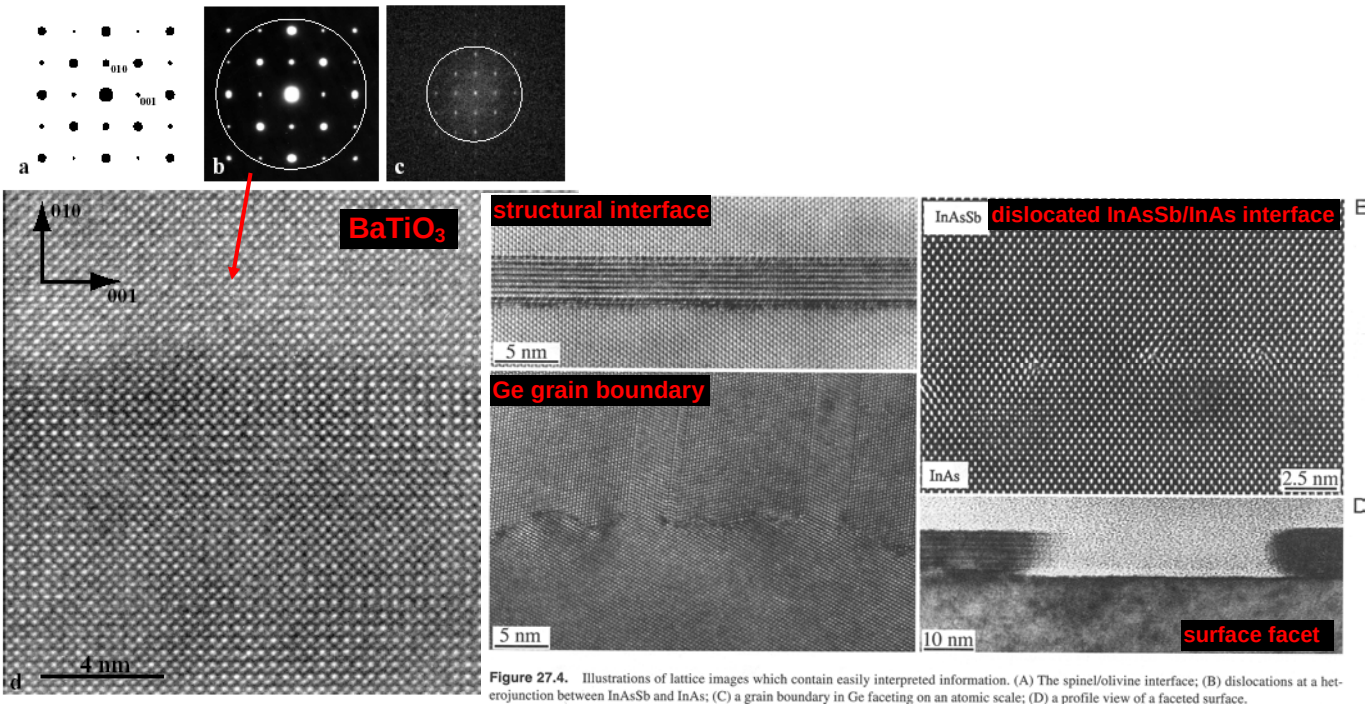

Figure 27.4. Illustrations of lattice images which contain easily interpreted information. (A) The spinel/olivine interface; (B) dislocations at a heterojunction between InAsSb and InAs; (C) a grain boundary in Ge faceting on an atomic scale; (D) a profile view of a faceted surface.

Fig. 10.1. a) schematic [100] zone axis pattern for $BaTiO_3$; b) experimental pattern with out line of diffraction aperture; c) computed diffractogram of the high resolution image in d). The aperture is represented as a white circle, and several diffraction spots can be seen outside the circle (e.g. 022 reflection), indicating non-linear image contributions. Images acquired at 400 kV in a JEOL 4000EX.

Transfer function and Scherzer Defocus

Like for optical microscopy, high resolution in TEM is determined by the transfer function, i.e., the high spatial frequency cut off of the transfer function that is characterized by $\chi(\boldsymbol{u})$.

Calculated TEM transfer functions (right):

For different spherical aberration C_s and different overfocus Δf above the sample:

» cut-off increases with:

(a) decreasing C_s
(b) has a maximum for a certain Δf_{Sch} = *"Scherzer focus"*

$$\Delta f_{Sch} = -1.2\ (C_s\ \lambda)^{1/2}$$

At this defocus value the resolution is given by:

$$\Delta r_{Sch} = 0.66\ (C_s\ \lambda^3)^{1/4}$$

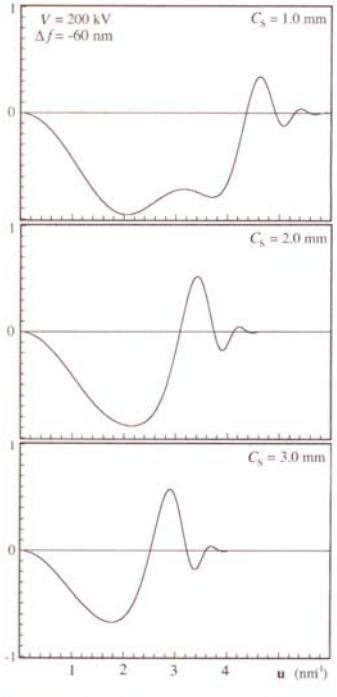

Figure 28.5. A series of sin χ curves calculated for different values of C_s. Remember 2 sin χ = T(u).

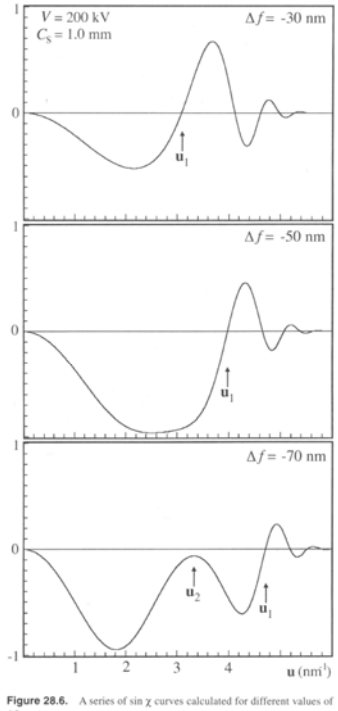

Figure 28.6. A series of sin χ curves calculated for different values of Δf.

Example: 200 kV: λ = 0.00251 nm with C_s = 1 mm » Δr_{Sch} = 2.36 Å.

To interpret high-resolution TEM images an image simulation is required, which has to be compared to the experimental images. Identification of atom positions not possible without image simulation !

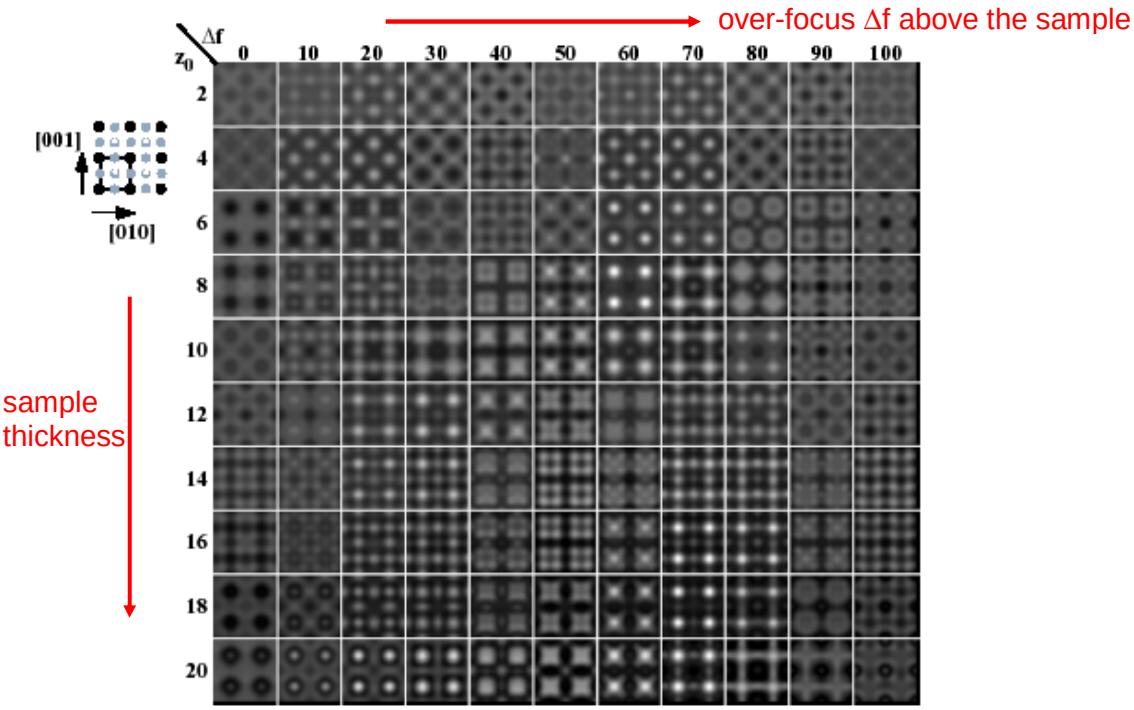

Fig. 10.30. HREM image simulation for the [100] zone axis of $BaTiO_3$, using the electron optical parameters stated in the text. The exit wave computation was carried out with the BWEW.f90 program, and the images were simulation with HREMExample.f90. All images use a common intensity scale.

1.8 Other Operation Modes

(i) Magnetic contrast (Lorentz) microscopy

Deflection of electrons by magnetic fields from the sample magnetization. Similar contrast mechanisms as in SEM, but with higher contrast due to the use of additional beam apertures.

(ii) STEM

When additional scan electronics, focusing optics and electron detectors are incorporated in a TEM, the same scanning electron operation modes and contrasts as in SEM can be achieved by STEM.

SE photomultiplier detector above the sample: Produces secondary electron images.
Large area Si detectors: Backscattered electron images with chemical contrast

In addition, also an electron detector can be used to record the transmitted electrons through the sample. In this case the same contrasts (strain, diffraction, etc.) as in the usual TEM mode can be obtained in STEM.

Generally, STEM images can be obtained with significantly higher resolution compared to SEM because:

- Better optics and lower lens aberrations in TEM results in smaller spot sizes.
- Thin specimen: Negligible remote SEII and BSII electron signal on the detector.

Resolution down to 1 nm achievable.

In STEM, in principle, also thick sample specimen can be investigated. The STEM then operates like a SEM.

STEM mode is also useful for performing cathodoluminescence imaging as well as chemical analysis in TEM using characteristic x-rays (EDX) or electron energy loss spectroscopy (EELS).

1.9 Summary

- TEM is the electron microscope analog to optical microscopy.
- **Caracteristic features**: Very small wavelengths due to high electron energy: 200 – 1000 keV, Very high resolution (atomic) down to 1 Å due to reduced lens aberrations and thin specimen.
- **Operation modes**:

  Diffraction mode: Diffraction patterns roughly correspond to plane cross section of reciprocal space, yields information about local crystal structure and orientation.

  Imaging mode: Contrast determined and controlled by selection of different parts of the diffraction pattern for image formation, bright field and dark field modes.
- **Contrast mechanisms**: Z-contrast, orientation contrast, structure contrast, strain contrast, magnetic contrast, phase contrast, etc. .
- TEM particular useful for high resolution imaging of crystal defects such as dislocations.
- **Atomically resolved images**: Difficult interpretation, must be based on image simulations.
- **STEM scanning mode**: Diffraction imaging as well as SE and BSE imaging like for SEM but higher resolution possible, combined with analytical methods such as EDX and EELS.